Journal of Non-Newtonian Fluid Mechanics 273 (2019) 104185

Contents lists available at ScienceDirect

Journal of Non-Newtonian Fluid Mechanics

journal homepage: www.elsevier.com/locate/jnnfm

Swimming with small and large amplitude waves in a confined liquid crystal

Madison S. Krieger[a], Saverio E. Spagnolie[b,*], Thomas R. Powers[c,d]

[a] Program for Evolutionary Dynamics, Harvard University, Cambridge, MA 02138 USA
[b] Department of Mathematics, University of Wisconsin-Madison, Madison, WI 53706 USA
[c] School of Engineering, Brown University, Providence, RI 02912 USA
[d] Department of Physics, Brown University, Providence, RI 02012 USA

A B S T R A C T

Boundaries can have a significant impact on the physics of microorganism locomotion. Here we examine the effects of confinement by a rigid boundary or symmetric channel on undulatory locomotion in an anisotropic fluid, treated as a nematic liquid crystal. The competition between hydrodynamics, fluid elasticity, and anchoring conditions results in a complex locomotion problem with unique transport properties. We examine this problem analytically using a well-known mathematical model, an infinite swimming sheet with small wave amplitude, and numerically for large amplitude waves using a modification of the immersed boundary method. For a prescribed stroke and strong planar anchoring in the narrow channel, we demonstrate that the swimming speed approaches its Newtonian value, though the power required to maintain the swimmer's speed depends on the properties of the liquid crystal. We also show that an unusual prograde swimming (in the direction of transverse wave propagation) theorized to exist at small wave amplitude persists at large amplitude, and that the presence of a sufficiently close boundary returns the swimming behavior to the more standard retrograde motion (opposite the direction of the traveling wave).

1. Introduction

The theory of swimming microorganisms is of importance to interdisciplinary topics spanning microbiology, medicine, and applied mathematics [1]. With the exception of marine microorganisms, locomotion largely occurs in confinement, and hydrodynamic forces induce long-range interactions between a shape-changing body and flexible or inflexible solid boundaries. The original works on an infinite waving sheet (the Taylor swimmer [2]) locomoting near an inflexible solid boundary in a Newtonian fluid showed that the presence of the wall tends to increase the swimming speed for a prescribed swimming stroke [3,4]. These works studied two complementary limits: the small-amplitude approximation in which the swimmer amplitude is small compared to the swimmer wavelength [3], and the lubrication approximation in which the swimmer wavelength is long relative to the distance to the wall [4]. Extensions of these studies have included the effects of confinement in isotropic complex fluids [5–7], on flagellar shapes [8], in large amplitude simulations [9,10], on helical waves [11,12], and with wall elasticity [7,13,14]. More generally, the behavior of finite-sized active particles near flat surfaces has seen considerable attention in both Newtonian [15–19] and non-Newtonian fluids [20,21]. Dynamics in confinement with more complex geometries (including funnels and gears) have resulted in particularly interesting trajectories [22–35]. For recent reviews of the field see Refs. [36–38]. In all of the works above the fluid has been assumed to be isotropic. In this article we study a Taylor swimmer near a surface in an anisotropic complex fluid.

A typical model for anisotropic fluids is a liquid crystal, which has orientational order but not positional order [39]. Recent experimental investigations have shown that self-propelled bacteria in a nematic liquid crystal swim along the molecular director field [40–42]. This principal behavior has been exploited to extract mechanical work in the transport of passive colloids [43,44], and shown to result in anomalous superdiffusion [45] and bacterial entrapment in topological defects [46]. In addition, this choice of medium is prompted by the commonalities between liquid crystals and several environments populated by bacteria, such as extracellular DNA suspensions [47] and flocks confined to very thin films, where recent experiments have revealed the existence of nematic order for dense populations [48]. Other biological environments which contain long biopolymers also show signs of liquid crystalline order, including various types of mucus [49–52].

Our previous work on locomotion in hexatic [53,54] and nematic [55] liquid crystals revealed novel properties which suggest that the extension to confined spaces may be of interest in both biological and technological applications. In the absence of confinement, tuning the material parameters of the liquid crystal was found to either enhance or reduce the swimming speed, even changing the direction of swimming for a given swimmer waveform. In particular, for certain sets of fluid properties the swimmer's waveform can remain stationary in the lab frame even though it is continuously passing a traveling wave along its body. In addition, this work suggests that an unconfined swimmer always induces a global volumetric flux in the fluid, which is so far unique to anisotropic fluids and suggests novel mechanisms for pumping which

* Corresponding author.
E-mail address: spagnolie@math.wisc.edu (S.E. Spagnolie).

https://doi.org/10.1016/j.jnnfm.2019.104185
Received 4 April 2019; Received in revised form 25 September 2019; Accepted 10 October 2019
Available online 11 October 2019
0377-0257/

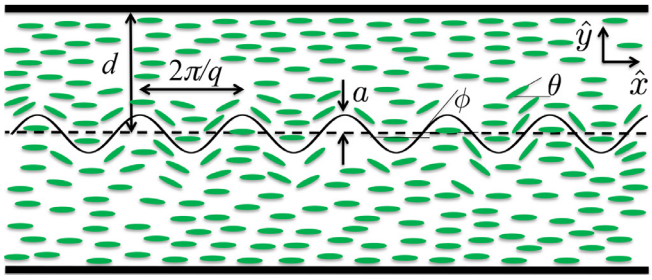

Fig. 1. Geometry of the confined locomotion problem in two-dimensions. An infinite sheet passes a traveling transverse wave of amplitude a, wavenumber q, and wavespeed $c = \omega/q$ along its body. The sheet is centered in a channel of width $2d$, so that when $a = 0$ the distance between the swimmer and the wall is d. The director field is locally represented as $\mathbf{n} = (\cos\theta, \sin\theta)$, and the tangent angle on the surface of the sheet is ϕ.

may find application in microfluidics [56–58]. This led to the design of a theoretical swimmer which instead of deforming its body via a traveling wave interacts with the liquid crystal instead via a traveling wave of preferred anchoring angle [55]. We therefore seek to understand how these effects may change when the system is placed under confinement.

The organization of the paper is as follows. In Section 2, we define our model for the Taylor swimmer and reprise the basic scaling for the small-amplitude and lubrication limits for swimming in a confined Newtonian liquid. We then introduce the equations of nematohydrodynamics to be solved in Section 3. The small-amplitude expansion is described and analyzed in Section 4, followed by analysis of the lubrication approximation in Section 5. In both the small-amplitude and long-wavelength limits, we find that the swimming speed approaches the isotropic Newtonian speed as the swimmer approaches the wall. We present a numerical method in Section 6, and compute solutions to the full nonlinear equations in Section 7 in order to examine large wave amplitudes and large director deformations arising from competing boundary conditions on both the swimmer body and the channel wall. Some closing remarks are given in Section 8.

2. Swimming in a confined Newtonian fluid

We begin by reviewing how a swimming microorganism in a Newtonian fluid at zero Reynolds number behaves in an unconfined fluid, and also how it behaves in a narrow channel. We consider a Taylor swimmer [2], or an infinite filament in two dimensions with a traveling wave of deformation, confined between two walls which are each at a distance d from the mid-line of the swimmer (Fig. 1). Initially, we consider the limit $d \to \infty$, so that the walls have no impact on the swimmer. Taylor solved this problem by expanding the Stokes equations and the no-slip boundary condition on the body of the swimmer in the small amplitude of the traveling wave. Given a traveling wave amplitude a, frequency ω, and wavenumber q, the governing approximation is $\varepsilon = aq \ll 1$. Perturbation theory then is used to derive the leading-order contribution to the swimming speed,

$$U_{\text{Taylor}} = \frac{1}{2}\varepsilon^2 c, \tag{1}$$

where c is the wave speed ($c = \omega/q$). Here, the swimmer travels opposite the direction of the traveling wave (retrograde motion), as is typical for undulatory swimmers such as mammalian spermatozoa.

When d is finite, there are three length scales in the problem: d, a, and q. As long as $a < d$, we may still usefully consider the case of small ε. Employing similar methods as Taylor, Reynolds [3] found the swimming speed at leading order in the confined case to be

$$U_{\text{Reynolds}} = \frac{1}{2}\varepsilon^2 c\left(\frac{\sinh^2(qd) + q^2d^2}{\sinh^2(qd) - q^2d^2}\right). \tag{2}$$

Note that for fixed a the swimming speed diverges for small qd as

$$U_{\text{Reynolds}} \sim \frac{3ca^2}{d^2}. \tag{3}$$

However, the divergence is cut off when $d \approx a$, since the calculation becomes invalid at $d = a$ as the swimmer in this case is in physical contact with the wall.

An alternative scheme for perturbative expansion was employed by Katz [4] (see also [59]), who used lubrication theory with the assumption of a long wavelength relative to the distance to the wall, or $\delta = qd \ll 1$, and found the swimming speed to be

$$U_{\text{Katz}} = \frac{3c}{2 + (d/a)^2} \tag{4}$$

to leading order in δ. The small wavenumber limit of U_{Reynolds} agrees with the small amplitude limit of U_{Katz}.

3. Governing equations for a nematic liquid crystal

We here present the governing equations for a nematic liquid crystal, along with reduced expressions for the two-dimensional system, relevant boundary conditions, and nondimensionalization. Our conventions for the field equations follow those of Landau and Lifshitz [60], specialized to two dimensions [55], where the velocity field is written as $\mathbf{v} = (u, v)$ and director field as $\mathbf{n} = (\cos\theta, \sin\theta)$. The elastic energy density for deformations of the director is the Frank energy,

$$\mathcal{F} = \frac{K_1}{2}(\boldsymbol{\nabla}\cdot\mathbf{n})^2 + \frac{K_2}{2}(\mathbf{n}\cdot\boldsymbol{\nabla}\times\mathbf{n})^2 + \frac{K_3}{2}[\mathbf{n}\times(\boldsymbol{\nabla}\times\mathbf{n})]^2, \tag{5}$$

where K_1 is the splay elastic constant, K_2 is the twist elastic constant, and K_3 is the bend elastic constant [60,61], and the two-dimensional nematic is assumed to be twist-free. The total free energy in the fluid (per unit length) is $E_f = \int \mathcal{F}\mathrm{d}x\mathrm{d}y$.

Equilibrium configurations of the director field are found by minimizing E_f subject to $|\mathbf{n}| = 1$. The stress corresponding to the elastic free energy $\mathcal{F}$ is

$$\sigma^{\mathrm{r}}_{ik} = -\Pi_{kl}\partial_i n_l - \frac{\lambda}{2}\left(n_i h_k + n_k h_i\right) + \frac{1}{2}\left(n_i h_k - n_k h_i\right), \tag{6}$$

where $\Pi_{ki} = \partial\mathcal{F}/\partial(\partial_k n_i)$, $\mathbf{h} = \mathbf{H} - \mathbf{n}(\mathbf{n}\cdot\mathbf{H})$ is the transverse part of the molecular field, $\mathbf{H} = -\delta E_f/\delta\mathbf{n}$, and repeated indices imply summation [39,60]. At equilibrium, $\mathbf{h} = \mathbf{0}$. Balancing torques on the directors implies the balance of elastic forces, $-\partial_i p_{\text{eq}} + \partial_j\sigma^{\mathrm{r}}_{ij} = 0$, as long as the pressure is equal to $p_{\text{eq}} = -\mathcal{F}$ [39]. The parameter λ is not a dissipative coefficient, but is related to the degree of order and the temperature of the sample. Rod-like molecules tend to have $\lambda > 0$, and disc-like molecules tend to have $\lambda < 0$. The parameter λ is sometimes known as the "tumbling parameter" since in simple shear flow the director tends to rotate if $\lambda < 1$, and align with the principal direction of shear if $\lambda \geq 1$ [61]. The tumbling parameter varies between $\lambda = 0.6$–0.9 [62] in disodium cromoglycate (DSCG), a lyotropic chromonic liquid crystal used in experiments on swimming microorganisms in liquid crystals [40,42,63].

Meanwhile, the director field has a preferential angle on the boundaries of the swimmer and the channel wall due to anchoring conditions. We will study the case of tangential anchoring, which is the case observed for the boundaries of microorganisms in DSCG [63], by including an additional energy density

$$\mathcal{F}_a = -W\int_0^{2\pi}\cos[2(\theta-\phi)]\mathrm{d}\ell - \bar{W}\int_0^{2\pi}\cos(2\theta)\mathrm{d}\ell_w, \tag{7}$$

where ϕ is the (time-dependent) tangent angle of the boundaries (the tangent angle is zero for a flat wall), W and $\bar{W}$ are anchoring strengths, and $\mathrm{d}\ell$ and $\mathrm{d}\ell_w$ are infinitesimal line elements along the swimmer and the wall, respectively.

The fluid's viscous stress response to deformation is approximated by incorporating terms linear in the strain rate that preserve $\mathbf{n} \to -\mathbf{n}$ symmetry. In an incompressible nematic, the deviatoric viscous stress [60,61] is

$$\boldsymbol{\sigma}^{\mathrm{d}} = 2\mu\mathsf{E} + 2\mu_1\mathbf{nn}(\mathbf{n}\cdot\mathsf{E}\cdot\mathbf{n}) + \mu_2(\mathbf{n}\mathsf{E}\cdot\mathbf{n} + \mathbf{n}\cdot\mathsf{E}\mathbf{n}), \tag{8}$$

with $\mathsf{E} = \left[\nabla\mathbf{v} + (\nabla\mathbf{v})^{\mathrm{T}}\right]/2$ the symmetric rate-of-strain tensor. The shear viscosity of an isotropic phase is μ, and μ_1 and μ_2 are viscosities arising from the anisotropy. The coefficients μ_1 and μ_2 can be negative, but the physical requirement that the power dissipation be positive yields bounds of $\mu > 0$, $\mu_2 > -2\mu$, and $\mu_1 + \mu_2 > -3\mu/2$. A particular case of interest is the parameter set $K_1 = K_3$, $\mu_1 = \mu_2 = 0$, and $\lambda = 0$, which is the limit of a hexatic liquid crystal [53].

The Cauchy momentum equation in the limit of small Reynolds number (the limit relevant to microorganism locomotion [64]) results in instantaneous force balance,

$$-\nabla p + \nabla \cdot \left(\boldsymbol{\sigma}^{\mathrm{d}} + \boldsymbol{\sigma}^{\mathrm{r}}\right) = \mathbf{0}, \tag{9}$$

and mass conservation is satisfied by demanding that the velocity field is divergence free, $\nabla \cdot \mathbf{v} = 0$. Torque balance is expressed by

$$\partial_t \mathbf{n} + \mathbf{v} \cdot \nabla\mathbf{n} - \frac{1}{2}(\nabla \times \mathbf{v}) \times \mathbf{n} = \lambda(\mathbf{I} - \mathbf{nn}) \cdot \mathsf{E} \cdot \mathbf{n} + \frac{1}{\gamma}\mathbf{h}, \tag{10}$$

where γ is a rotational or twist viscosity and $\mathbf{nn}$ is a dyadic product [60,61]. In DSCG, γ/μ ranges from roughly 5 to 50 [65]. The viscous torque arising from the rotation of the director relative to the local fluid rotation balances with that from the viscous torque through E and elastic torque through $-\mathbf{h}$. The equations of motion in the two-dimensional system of interest are presented in Appendix A. For the duration we will work in the rest frame of the swimmer.

The no-slip velocity boundary condition is applied on the swimmer surface and the solid boundary. The swimming body is modeled as an infinite sheet undergoing a prescribed transverse sinusoidal undulation of the form

$$Y(x,t) = a\sin(qx - \omega t), \tag{11}$$

measured in the frame moving with the swimmer. We will focus only on transverse waves. The boundary conditions on the fluid flow are then

$$\mathbf{v}(x, Y(x,t)) = \left(0, \frac{\partial Y}{\partial t}(x,t)\right), \tag{12}$$

$$\mathbf{v}(x, \pm d) = (U, 0), \tag{13}$$

where $-U$ is the (signed) swimming speed which must be determined. The system is closed by demanding that the swimming body remains force-free at all times.

4. Small-amplitude expansion

We begin by exploiting the assumption of small wave amplitude, $\epsilon = aq \ll 1$ to perform a semi-analytical calculation of the swimming speed. For now we also assume that the swimmer is sufficiently well separated from the wall, $a \ll d$. The passage of transverse waves in a Newtonian fluid results in retrograde swimming, where the swimming body moves in the direction opposite that of the traveling wave (here, then, with $U > 0$) [2]. Among the unusual behaviors theorized for motion in a liquid crystal, we showed in Ref. [55] that if the rotational viscosity γ is large compared to the shear viscosity μ, then a swimmer in an unbounded liquid crystal instead performs prograde swimming, self-propulsion in the same direction as the direction of wave propagation ($U < 0$).

In this section we show that as the distance to a nearby wall decreases, there is an increasing contribution to the swimming velocity in the direction opposite to the direction of the prescribed swimmer waveform. Thus, in a fluid with a large rotational viscosity, a swimmer will swim in the same direction as the waveform far from the wall, but slow down, reverse direction, and then swim faster and faster as the distance to the wall decreases.

For completeness we provide a brief outline of the calculation of the swimming speed to second-order in amplitude; the derivation of these steps and the fine details can be found in Ref. [55].

4.1. Nondimensionalization

We treat x, y, and t as dimensionless variables by measuring length in units of q^{-1} and time in units of ω^{-1}. Dimensionless viscosities are defined by $\mu_1^* = \mu_1/\mu$, $\mu_2^* = \mu_2/\mu$ and $\gamma^* = \gamma/\mu$. The swimmer shape in dimensionless form is given by

$$Y = \epsilon \sin(x - t), \tag{14}$$

where $\epsilon = aq$, and in this section we assume $\epsilon \ll 1$.

The Frank elasticity of the liquid crystal leads to a relaxation time, defined as $\tau = \mu/(K_3 q^2)$. For small-molecule liquid crystals, typical values are $\mu \approx 10^{-2}$ Pa s and $K_3 \approx 10^{-11}$ N; hence, on the length scale of typical flagellar wavelengths, for which $q \approx 1\ \mu\mathrm{m}^{-1}$, the relaxation time is $\tau \approx 1$ ms. Comparing the typical viscous stress in Eq. (8) with the typical elastic stress in Eq. (6), we define the Ericksen number [61], $\mathrm{Er} = \omega\tau$, or

$$\mathrm{Er} = \frac{\mu\omega}{K_3 q^2}. \tag{15}$$

The beat frequencies and wavenumbers of cilia and flagella vary widely [66,67], and for experiments on bacteria in liquid crystals the Ericksen number can range from $\mathrm{Er} \approx 10^{-1}$ [40,63] to $\mathrm{Er} \approx 10^{1}$ [42]. Finally, the ratio of Frank constants is denoted by $K_r = K_1/K_3$, and we define $U^* = U/c$ (with $c = \omega/q$ the wavespeed), and $Q^* = Q/(\omega\epsilon^2/q^2)$, the dimensionless volumetric flux.

4.2. First order in amplitude

It is convenient to enforce fluid incompressibility by introducing the stream function $\psi(x, y)$, which is related to the velocity via $\mathbf{v} = \nabla^{\perp}\psi = (\psi_y, -\psi_x)$. Expanding the stream-function as $\psi = \epsilon\psi^{(1)} + \epsilon^2\psi^{(2)} + \ldots$ and the director angle as $\theta = \epsilon\theta^{(1)} + \epsilon^2\theta^{(2)} + \ldots$, the governing equations to first order in ϵ are

$$\nabla^4\psi^{(1)} + \frac{4\mu_1^*}{2+\mu_2^*}\partial_x^2\partial_y^2\psi^{(1)} + \frac{1}{(2+\mu_2^*)\mathrm{Er}} \times \left\{(1+\lambda)\partial_x^4\theta^{(1)} + \left[K_r(1+\lambda) + 1 - \lambda\right]\partial_x^2\partial_y^2\theta^{(1)} + K_r(1-\lambda)\partial_y^4\theta^{(1)}\right\} = 0, \tag{16}$$

$$\partial_t\theta^{(1)} + \frac{1+\lambda}{2}\partial_x^2\psi^{(1)} + \frac{1-\lambda}{2}\partial_y^2\psi^{(1)} - \frac{1}{\mathrm{Er}\,\gamma^*}\left(\partial_x^2\theta^{(1)} + K_r\partial_y^2\theta^{(1)}\right) = 0. \tag{17}$$

These equations are solved by sums of complex exponentials $\psi^{(1)} = \Re[\tilde{\psi}^{(1)}]$ and $\theta^{(1)} = \Re[\tilde{\theta}^{(1)}]$, where

$$\tilde{\psi}^{(1)} = \sum_{j=1}^{6} c_j e^{r_j y + \mathrm{i}(x-t)}, \quad \tilde{\theta}^{(1)} = \sum_{j=1}^{6} d_j e^{r_j y + \mathrm{i}(x-t)}. \tag{18}$$

The characteristic decay rates r_j are found by inserting (18) into (16) and (17), leading to a cubic equation for $m = r_j^2$, $A_3 m^2 + A_2 m^2 + A_1 m + A_0 = 0$, where [1]

$$\begin{aligned}
A_3 &= K_r\left[\gamma^*(-1+\lambda)^2 + 4 + 2\mu_2^*\right],\\
A_2 &= A_0 + 4\gamma^*\lambda + 2K_r\left[\gamma^*\left(-1+\lambda^2\right) - 4 - 4\mu_1^* - 2\mu_2^*\right],\\
A_1 &= K_r\left[\gamma^*(1+\lambda)^2 + 2(2+\mu_2^*)\right] + 2\left(4 + 4\mu_1^* + 2\mu_2^*\right)\\
&\quad + \gamma^*\left[1 - \lambda^2 - 2\mathrm{iEr}(2 + 2\mu_1^* + \mu_2^*)\right],\\
A_0 &= -2\left(2+\mu_2^*\right) + \gamma^*\left[-(1+\lambda)^2 + 2\mathrm{iEr}(2+\mu_2^*)\right].
\end{aligned} \tag{19}$$

The relationship between the coefficients c_j and d_j is determined by the governing equations for the stream function and the angle field, resulting in

$$d_j = c_j \frac{\mathrm{Er}\,\gamma^*\left[1 + \lambda - (1-\lambda)r_j^2\right]}{2\left(1 - K_r r_j^2 - \mathrm{i}\,\mathrm{Er}\,\gamma^*\right)}. \tag{20}$$

[1] Correcting here a typographical error in Ref. [55] in which a spurious factor of m appeared in front of the equation defining A_1.

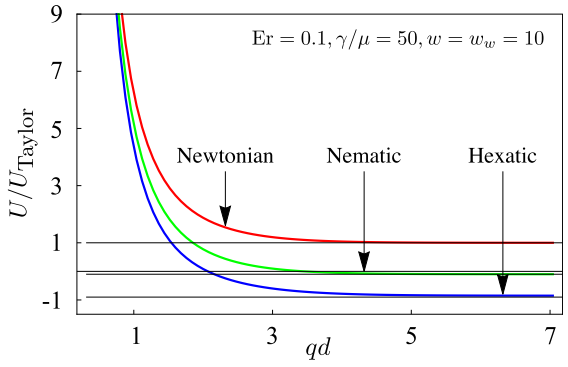

Fig. 2. Swimming speed for a swimmer near a wall (relative to the Newtonian swimming speed far from the wall), in the limit of small amplitude $aq \ll 1$. For the nematic plot, $K_r = K_1/K_3 = 1.2$, $\lambda = 0.6$, and $\mu_1/\mu = \mu_2/\mu = 1$. Both liquid crystalline phases have $\gamma/\mu = 50$, Er $= 0.1$, and strong parallel anchoring is enforced both on the body of the swimmer and on the solid boundary. Horizontal black lines indicate the unconfined swimming speeds from [55].

The rest of the coefficients are determined by the boundary conditions, which to second order in the angle field are written as

$$-\partial_y\theta + w(\theta - \partial_x Y)\Big|_{y=Y(x,t)} = 0, \tag{21}$$

$$-\partial_y\theta + \bar{w}\theta\Big|_{y=\pm qd} = 0, \tag{22}$$

where $w = W/(qK_1)$ and $\bar{w} = \bar{W}/(qK_1)$ are dimensionless anchoring strengths on the swimmer and wall, respectively. The swimming speed has no contribution at first order: with $U = \varepsilon U^{(1)} + \varepsilon^2 U^{(2)} + \dots$, taking $\varepsilon \to -\varepsilon$ amounts to a simple phase shift of the waveform, thus demanding that $U^{(1)} = 0$. We must therefore proceed to second order in the amplitude ε in order to find the leading order contribution to the swimming speed.

4.3. Second order in amplitude

Although the small-amplitude swimming speed $U_{\rm sa}$ is a second-order quantity in ε, it is possible to write it as an integral over quadratic combinations of first-order quantities:

$$U_{\rm sa} = -\left\langle Y\partial_y v_x^{(1)}\right\rangle|_{y=0} - \alpha\int_0^{qd}\left[\gamma^*(1-\lambda)g + (2+\mu_2^*)yf\right]{\rm d}y, \tag{23}$$

where $\alpha = 2[\gamma^*(1-\lambda)^2 + 2(2+\mu_2^*)]^{-1}$, and the operation $\langle\cdot\rangle$ indicates that an average of the bracketed quantity is to be performed over one swimmer wavelength in x. Note that while here we have obtained this expression by simply solving the equations, in general this can also be accomplished via the reciprocal theorem [68]. The first-order quantities f and g are given by

$$f = \frac{k_1}{\rm Er}\left\langle \partial_x\theta^{(1)}\partial_y^2\theta^{(1)}\right\rangle + \frac{4\mu_1^*}{2+\mu_2^*}\left\langle \nabla\theta^{(1)}\cdot\partial_y\mathbf{v}^{(1)}\right\rangle, \tag{24}$$

$$g = \left\langle \mathbf{v}^{(1)}\cdot\nabla\theta^{(1)}\right\rangle - 2\lambda\left\langle \partial_x\theta^{(1)}v_x^{(1)}\right\rangle - \frac{k_2}{\gamma^*\,{\rm Er}}\left\langle \partial_y\theta^{(1)}\partial_x\theta^{(1)}\right\rangle, \tag{25}$$

with $k_1 = [K_r(1+\lambda) + 1 - \lambda]/(2+\mu_2^*)$ and $k_2 = K_r - 1$. The results are plotted in Fig. 2. When qd is large, we recover the results of Refs. [53,55] for swimming in an infinite fluid. As $qd \to 0$, the dependence on liquid crystalline parameters is overwhelmed by the diverging Newtonian component; in the Newtonian limit, we recover the speed found by Reynolds [3], given in Eq. (2).

Notably, for rheological parameters that lead to negative U in an unbounded fluid (in particular, large γ/μ), the swimming speed does not diverge to negative infinity, but instead reverses and passes through positive swimming speeds on its way to positive infinity. The nature of the blow-up as $qd \to 0$ is described exactly by Eq. (2) – terms depending on liquid crystalline properties remain $\mathcal{O}(1)$ for all qd, whereas Newtonian terms blow up proportional to $(qd)^{-2}$. The volumetric flux Q^* of fluid pumped by the swimmer also decays to zero as $qd \to 0$.

5. Small-wavenumber (lubrication) expansion

Since the expressions for the swimming speed near a wall for a low-amplitude swimmer are too unwieldy to display, we turn to the lubrication approximation to try to get more insight into the problem in the limit when $\delta = qd$ is small but a/d can take any value less than one. We work in the limit in which the anchoring strength is so strong that the director is always parallel to the swimmer surface, which is achieved in practice for $w = \mathcal{O}(10)$ or above. This problem has been treated for swimming in a Newtonian fluid [4,59,69], and in an isotropic viscoelastic fluid [6]. The lubrication approach has also been applied to the spreading of liquid crystal droplets; see e.g. [70] and references therein.

Because we use a different choice for nondimensionalization than in Section 4, we define new dimensionless variables, measuring length along x by the wavelength, and length along y by the gap between the swimmer and the wall: $\tilde{x} = qx$, $\tilde{y} = y/d$, $u = c\tilde{u}$, $v = \delta c\tilde{v}$, and $\tilde{t} = \omega t$. The choices for the relative scaling of the velocity components u and v are the usual ones in lubrication theory, dictated by incompressibility. Balance of viscous forces with pressure gradients suggests $\tilde{p} = qd^2p/(\mu c)$. Also, the strong anchoring condition forces the director angle θ to equal the slope of the swimmer at the swimmer surface. Since this slope is small in the lubrication limit, we define $\theta = \delta\tilde{\theta}$, where $\tilde{\theta}$ is expected to be of order unity.

Next, we write the governing equations in the dimensionless variables. Many of the terms drop out to leading order in δ. For example, the Frank free energy density is dominated by the splay contribution when $\delta \ll 1$,

$$\mathcal{F} \approx \frac{K_1}{2}\frac{\delta^2}{d^2}\left(\frac{\partial\tilde{\theta}}{\partial\tilde{y}}\right)^2, \tag{26}$$

leading to a greatly simplified molecular field $\mathbf{h}$. Similarly, the stresses have only a few terms at leading order in δ:

$$\boldsymbol{\sigma}^{\rm r} = \frac{\delta}{d^2}\frac{K_1}{2}\frac{\partial^2\tilde{\theta}}{\partial\tilde{y}^2}\begin{pmatrix}\mathcal{O}(\delta) & 1-\lambda\\ -1-\lambda & \mathcal{O}(\delta)\end{pmatrix},\quad \boldsymbol{\sigma}^{\rm d} = \frac{\mu c}{d}\frac{\partial\tilde{u}}{\partial\tilde{y}}\begin{pmatrix}\mathcal{O}(\delta) & 2+\mu_2^*/2\\ 2+\mu_2^*/2 & \mathcal{O}(\delta)\end{pmatrix}. \tag{27}$$

Balancing moments and forces leads to the lubrication equations for a nematic,

$$\frac{1-\lambda}{2}\frac{\partial\tilde{u}}{\partial\tilde{y}} - \frac{1}{\gamma^*}\frac{K_1}{K_3}\frac{1}{\rm Er}\frac{\partial^2\tilde{\theta}}{\partial\tilde{y}^2} = 0, \tag{28}$$

$$-\frac{\partial\tilde{p}}{\partial\tilde{x}} + \left(1+\frac{\mu_2^*}{2}\right)\frac{\partial^2\tilde{u}}{\partial\tilde{y}^2} + \frac{1-\lambda}{2{\rm Er}}\frac{K_1}{K_3}\frac{\partial^3\tilde{\theta}}{\partial\tilde{y}^3} = 0, \tag{29}$$

$$-\frac{\partial\tilde{p}}{\partial\tilde{y}} = 0, \tag{30}$$

$$\frac{\partial\tilde{u}}{\partial\tilde{x}} + \frac{\partial\tilde{v}}{\partial\tilde{y}} = 0. \tag{31}$$

The no-slip boundary conditions on the fluid are

$$(\tilde{u},\tilde{v})\Big|_{\tilde{y}=\pm1} = (\tilde{U},0), \tag{32}$$

$$(\tilde{u},\tilde{v})\Big|_{\tilde{y}=(a/d)\sin(\tilde{x}-\tilde{t})} = \left(0, -\frac{a}{d}\cos(\tilde{x}-\tilde{t})\right), \tag{33}$$

where $\tilde{U}$ is the unknown dimensionless swimming speed. The strong-anchoring boundary conditions on the director field are

$$\tilde{\theta}(\tilde{x},1) = 0, \tag{34}$$

$$\tilde{\theta}\left(\tilde{x}, \frac{a}{d}\sin(\tilde{x}-\tilde{t})\right) = \frac{a}{d}\cos(\tilde{x}-\tilde{t}). \tag{35}$$

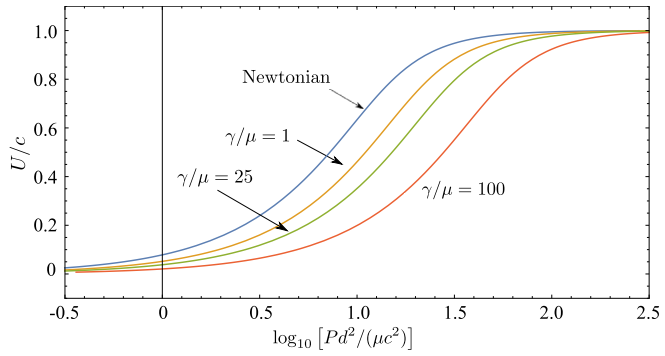

Fig. 3. Dimensionless power consumption in the lubrication limit versus swimming speed, for $K_1 = K_3$, $\mu = \mu_2$, $\lambda = 0.75$, strong parallel anchoring on all surfaces and $\gamma = 1$ (gold), $\gamma = 25$ (green), and $\gamma = 100$ (red). The blue line corresponds to the Newtonian case. Note that the value of the Ericksen number is not given, as the Ericksen number disappears from the dynamics in Eqs. (36)–(37). (For interpretation of the references to colour in this figure legend, the reader is referred to the web version of this article.)

Eliminating the angle field via the torque-balance Eq. (28) leads to

$$-\frac{\partial \tilde{p}}{\partial \tilde{x}} + \beta \frac{\partial^2 \tilde{u}}{\partial \tilde{y}^2} = 0, \tag{36}$$

where

$$\beta = 1 + \frac{\mu_2^*}{2} + \frac{\gamma^*(1-\lambda)^2}{4}. \tag{37}$$

Note that the Ericksen number disappears completely from the dynamics in the lubrication limit. Furthermore, since the Eqs. (36) and (30) are identical to the lubrication equations for isotropic Stokes flow with dimensionless pressure $\tilde{p}$ replaced by $\tilde{p}/\beta$, the flow field and swimming velocity are the same as in the isotropic case. For completeness, we include the derivation of the flow field and swimming velocity in Appendix B.

Solving the equations yields the dimensional swimming speed which was found by Katz [4], given in Eq. (4). The time-averaged volumetric flux, a hallmark of unconfined swimming in a liquid crystal, also vanishes in the lab frame. Therefore, we find that for a nematic liquid crystal with strong planar anchoring conditions, the swimming speed and flux are the same as in the isotropic Newtonian case.

However, the power consumed by the swimmer is not the same as in a Newtonian fluid. The power dissipated in the fluid can be written as

$$\mathcal{P} = \boldsymbol{\sigma}^d : \mathsf{E} + \frac{1}{\gamma}|\mathbf{h}|^2, \tag{38}$$

with the convention $\mathbf{A} : \mathbf{B} = A_{ij}B_{ij}$. Expanding in powers of δ and using the equations of motion to simplify gives the leading-order contribution,

$$\mathcal{P} = \left(1 + \frac{\mu_2}{2\mu}\right)\left[1 + \frac{\gamma(1-\lambda)^2}{4\mu}\right]\mathcal{P}_0, \tag{39}$$

where $\mathcal{P}_0 = (\partial u/\partial y)^2$ is the isotropic Newtonian power density. Writing $P = \int_0^{2\pi} \mathrm{d}\tilde{x} \int_{\tilde{Y}}^1 \mathrm{d}\tilde{y}\, \mathcal{P}$, and noting that

$$P_0 = \int_0^{2\pi} \mathrm{d}\tilde{x} \int_{\tilde{Y}}^1 \mathrm{d}\tilde{y}\, \mathcal{P}_0 = \frac{12\pi\tilde{a}^2}{\sqrt{1-\tilde{a}^2}(1+2\tilde{a}^2)}, \tag{40}$$

where $\tilde{a} = a/d$, we plot the ratio of nondimensionalized speed and nondimensionalized power for several liquid crystal parameters in Fig. 3. In the presence of the liquid crystal, the swimmer must inject more power per unit wavelength into the fluid to swim at the same speed, consistent with earlier results for a swimmer in an unbounded liquid crystal [53].

6. An immersed boundary method for flowing nematic liquid crystals

To compute the dynamics of the flowing liquid crystal and its coupling to the swimmer and boundaries we develop an adaptation of the classical immersed boundary method [71], which has been applied to similar swimming problems in viscoelastic fluids [7,72–76]. In order to include anchoring conditions of arbitrary strength we include an extra volumetric torque in the molecular field, writing

$$h = \nabla^2\theta + h^a(\theta), \tag{41}$$

$$h^a(\theta) = \int_{\partial\Omega} w(\mathbf{X}(s)) \sin\left(\phi(\mathbf{X}(s)) - \theta\right)\delta(\mathbf{x} - \mathbf{X}(s))\, ds, \tag{42}$$

where the boundary surface (both swimmer and wall), denoted by $\partial\Omega$, is parameterized by $\mathbf{X}(s) = (X(s), Y(s))$ with s the arc-length, $w(\mathbf{X})$ the dimensionless anchoring strength, and $\phi = \tan^{-1}(Y_s/X_s)$ the tangent angle (the preferred director angle for the assumed planar anchoring conditions). The elastic force density on the fluid is modified to include the anchoring contributions, resulting in

$$\begin{aligned}\mathbf{f}_e(\theta) = \nabla\cdot(\boldsymbol{\sigma}^r + \boldsymbol{\sigma}^a) = -\nabla^2\theta\,\nabla\theta - \frac{1}{2}\nabla(|\nabla\theta|^2) + (\nabla^2\theta + h^a)\nabla\cdot\mathbf{R}(\theta)\\ + \mathbf{R}(\theta)\cdot\nabla(\nabla^2\theta + h^a) + \nabla^\perp h^a(\theta),\end{aligned} \tag{43}$$

with $\mathbf{R}$ defined in Eq. (A.2), and $\nabla^\perp = \hat{\mathbf{x}}\partial_y - \hat{\mathbf{y}}\partial_x$. Finally, the director field evolution equation is modified to

$$\begin{aligned}\theta_t + \mathbf{v}\cdot\nabla\theta + \frac{1}{2}(u_y - v_x) = \lambda\left(\frac{\cos 2\theta}{2}(u_y + v_x) - \sin 2\theta\, u_x\right)\\ + \frac{1}{\gamma^*\,\mathrm{Er}}\left(\nabla^2\theta + h^a(\theta)\right).\end{aligned} \tag{44}$$

In the immersed boundary method the delta function is replaced by a discrete delta function with finite but compact support, and is chosen to ensure moment balance conditions that attempt to remove the dependence on grid location. Here we use the original discrete delta function from Ref. [77] with a four-point footprint in each dimension:

$$\delta_h(\mathbf{x}) = \frac{1}{\Delta x\Delta y} d_h\left(\frac{x}{\Delta x}\right) d_h\left(\frac{y}{\Delta y}\right), \tag{45}$$

where

$$d_h(r) = \begin{cases} \frac{1}{8}\left(3 - 2r + \sqrt{1 + 4r - 4r^2}\right) & 0 \le |r| < 1,\\ \frac{1}{8}\left(5 - 2r - \sqrt{-7 + 12r - 4r^2}\right) & 1 \le |r| < 2,\\ 0 & |r| \ge 2.\end{cases} \tag{46}$$

Spreading operators which carry information from the body onto the fluid, and vice versa, are then defined as

$$S_n^h[\mathbf{F}(\mathbf{X})] = \int_{\partial\Omega} \mathbf{F}(\mathbf{X})\delta_h(\mathbf{x} - \mathbf{X}_n(s))\, ds, \tag{47}$$

$$(S_h^n)^*[\mathbf{f}(\mathbf{x})] = \int_\Omega \mathbf{f}(\mathbf{x})\delta_h(\mathbf{x} - \mathbf{X}_n)\, dV, \tag{48}$$

where the subscript 'n' indicates that the surface $\mathbf{X}_n$ over which the integral is performed may differ from the surface $\mathbf{X}$ on which the function $\mathbf{F}$ is defined. For a given geometry (in practice, at the beginning of each timestep), we create sparse matrices representing the spreading operation, and we also form the sparse operator $S_h^n(S_h^n)^*$. Spreading is achieved using sparse matrix-vector multiplication for the duration of the timestep. Precomputing in this way makes the computational cost of spreading information to and from the surface negligible relative to other aspects of the time-stepping algorithm, which we presently describe.

The Leslie–Ericksen equations are advanced using semi-implicit time-stepping with a similar technique to that discussed in Ref. [78], discretizing in time as follows, where superscripts indicate the timestep, e.g. $\mathbf{v}^n = \mathbf{v}(t = t_n)$:

$$-\nabla p^{n+1} + \nabla\cdot\boldsymbol{\sigma}^v\left(\mathbf{v}^{n+1}; \tilde{\theta}^{n+1}\right) + \mathbf{f}_e\left(\theta^{n+1}; \tilde{\theta}^{n+1}\right) = -S_h^n\left[\mathbf{F}(\mathbf{X}^{n+1})\right], \tag{49}$$

$$\nabla \cdot \mathbf{v}^{n+1} = 0, \tag{50}$$

$$\theta^{n+1} + \frac{\Delta t}{2}\left(u_y^{n+1} - v_x^{n+1}\right) - \frac{\Delta t}{\gamma' \,\mathrm{Er}} h\left(\theta^{n+1}\right) = \theta^n + \Delta t\, N\left(\tilde{\mathbf{v}}^{n+1}, \tilde{\theta}^{n+1}\right), \tag{51}$$

$$\mathbf{X}^{n+1} = \mathbf{X}^n + \Delta t (S_h^n)^* \left[\mathbf{v}^{n+1}\right], \tag{52}$$

where we have defined

$$N(\mathbf{v}, \theta) = \lambda\left(\frac{\cos 2\theta}{2}(u_y + v_x) - \sin 2\theta\, u_x\right) - \mathbf{v} \cdot \nabla\theta, \tag{53}$$

$$\begin{aligned}\mathbf{f}_e\left(\theta^{n+1}; \tilde{\theta}^{n+1}\right) = &-\nabla\tilde{\theta}^{n+1}\nabla^2\theta^{n+1} + \nabla \cdot \mathbf{R}(\tilde{\theta}^{n+1})h(\theta^{n+1}) \\ &+ \mathbf{R}\left(\tilde{\theta}^{n+1}\right) \cdot \nabla h\left(\theta^{n+1}\right) + \nabla^\perp h^a\left(\theta^{n+1}\right),\end{aligned} \tag{54}$$

$$h(\theta^{n+1}) = \nabla^2\theta^{n+1} + w(\mathbf{X}^{n+1}) S_h^n\left[\phi(\mathbf{X}^{n+1}) - (S_h^n)^*\theta^{n+1}\right]. \tag{55}$$

The quantities $\tilde{\mathbf{v}}^{n+1} = 2\mathbf{v}^n - \mathbf{v}^{n-1}$ and $\tilde{\theta}^{n+1} = 2\theta^n - \theta^{n-1}$ are extrapolations to time t_{n+1} from information at previous time-steps. We have included in Eq. (49) a surface force density $\mathbf{F}(\mathbf{X})$ associated with the boundary material properties, to be described below. This force is computed at the advance time t_{n+1}, but is spread onto the surrounding fluid at the previous surface location (the semi-implicit approximation). The inclusion of a second surface is straight-forward in this approach.

It is convenient to define an auxiliary pressure p_* and velocity field $\mathbf{v}_*$ with the properties that $p = -\mathrm{Er}\nabla^2 p_*$ and $\mathbf{v} = \mathbf{v}_* - \nabla p_*$, for then $-\nabla p + \mathrm{Er}\nabla^2\mathbf{v} = \mathrm{Er}\nabla^2\mathbf{v}_*$, which removes the pressure from the momentum balance equation [79,80]. Using $\nabla \cdot \mathbf{v} = 0$ we find that $\nabla^2 p_* = \nabla \cdot \mathbf{v}_*$, and $\mathbf{v} = (\mathbf{I} - \nabla(\nabla^2)^{-1}\nabla\cdot)\mathbf{v}_*$. Eq. (49)–(52) may then be written as a large linear system,

$$\begin{pmatrix} \mathcal{L}_{v_* v_*} & \mathcal{L}_{v_*\theta} \\ \mathcal{L}_{\theta v_*} & \mathcal{L}_{\theta\theta} \end{pmatrix} \begin{pmatrix} \mathbf{v}_*^{n+1} \\ \theta^{n+1} \end{pmatrix} = \mathbf{A}(\mathbf{X}^{n+1}) + \mathbf{B}, \tag{56}$$

where (with care in distinguishing the auxiliary velocity field $\mathbf{v}_*$ from the true velocity field $\mathbf{v}$),

$$\mathcal{L}_{v_* v_*}\mathbf{v}_*^{n+1} = \mathcal{L}_{vv}\left(\mathbf{I} - \nabla(\nabla^2)^{-1}\nabla\cdot\right)\mathbf{v}_*^{n+1} = \nabla \cdot \boldsymbol{\sigma}^v\left(\mathbf{v}^{n+1}; \tilde{\theta}^{n+1}\right), \tag{57}$$

$$\begin{aligned}\mathcal{L}_{v_*\theta}\theta^{n+1} = &-\nabla\tilde{\theta}^{n+1}\left(\nabla^2\theta^{n+1}\right) + \nabla \cdot \mathbf{R}\left(\tilde{\theta}^{n+1}\right)\left(\nabla^2\theta^{n+1} - wS_h^n(S_h^n)^*\theta^{n+1}\right) \\ &+ \mathbf{R}(\tilde{\theta}^{n+1}) \cdot \nabla\left(\nabla^2\theta^{n+1} - wS_h^n(S_h^n)^*\theta^{n+1}\right),\end{aligned} \tag{58}$$

$$\mathcal{L}_{\theta v_*}\mathbf{v}_*^{n+1} = \mathcal{L}_{\theta v}\left(\mathbf{I} - \nabla(\nabla^2)^{-1}\nabla\cdot\right)\mathbf{v}_*^{n+1} = \frac{\Delta t}{2}(u_y^{n+1} - v_x^{n+1}), \tag{59}$$

$$\mathcal{L}_{\theta\theta}\theta^{n+1} = \theta^{n+1} - \frac{\Delta t}{\gamma' \,\mathrm{Er}}\left(\nabla^2\theta^{n+1} - wS_h^n(S_h^n)^*\theta^{n+1}\right), \tag{60}$$

and

$$\mathbf{A}(\mathbf{X}^{n+1}) = \begin{pmatrix} -S_h^n\left[\mathbf{F}(\mathbf{X}^{n+1})\right] - w\nabla\cdot\mathbf{R}\left(\tilde{\theta}^{n+1}\right)S_h^n\left[\phi(\mathbf{X}^{n+1})\right] - w\mathbf{R}\left(\tilde{\theta}^{n+1}\right)\cdot\nabla\, S_h^n\left[\phi(\mathbf{X}^{n+1})\right] \\ \dfrac{w\Delta t}{\gamma' \,\mathrm{Er}}\, S_h^n\left[\phi(\mathbf{X}^{n+1})\right] \end{pmatrix}, \tag{61}$$

$$\mathbf{B} = \begin{pmatrix} \mathbf{0} \\ \theta^n + \Delta t N\left(\tilde{\mathbf{v}}^{n+1}, \tilde{\theta}^{n+1}\right) \end{pmatrix}. \tag{62}$$

The fluid domain is taken to be periodic with dimensions $L_x \times L_y$, and we define the grid $(x_j, y_k) = (jh_x, kh_y)$ with $j = 0, 1, 2, \ldots, N_x - 1$, $k = 0, 1, 2, \ldots, N_y - 1$, and $(h_x, h_y) = (L_x/N_x, L_y/N_y)$. Time is discretized uniformly with step-size Δt, and we define $t_n = n\Delta t$. The immersed body is discretized by specifying its location at equally-spaced parameterization coordinates $s_m \in [0, 2\pi)$, with $m = 0, 1, \ldots, M - 1$. Typical values for the simulations to come are $(L_x, L_y) = (2\pi, 4\pi)$, $(N_x, N_y, M) = (32, 64, 64)$, and $\Delta t = 10^{-4}$. Resolution studies show slow convergence of averaged quantities and the swimming speed; the immersed boundary method is known to be delicate in the context of complex fluids, and we direct the reader to recent work on new modifications for improvement in Refs. [81,82].

We confine our attention to periodic boundary conditions, and a pseudo-spectral method [83] is used to solve the Leslie–Ericksen system, Eq. (56). With periodic boundary conditions imposed the velocity field is defined only up to a constant mean velocity which we denote by $\mathbf{v_c}$. Writing the velocity field instead as $\mathbf{v} + \mathbf{v_c}$, where $\mathbf{v}$ is the mean-free part of the velocity which satisfies the equations of motion above, we close the system by demanding that the net force in a periodic domain is zero. A marker-and-cell (MAC) method implementation showed no significant differences in either performance or in the results of the simulations. The system recast in a vorticity-stream function formulation also showed no appreciable differences in the results, but the approach taken here can be more easily extended to three-dimensions.

Instead of forming the matrix on the left-hand side of (56), the linear system is solved (for a given $\mathbf{X}^{n+1}$) using the generalized minimum residual (GMRES) method. For a preconditioner we solve the same system as above but replacing $\tilde{\theta}^{n+1}$ with 0, and constructing a sparse linear operator which is rapidly inverted at each iteration of GMRES. This preconditioner is only formed one time only and then used for all future simulations on the same domain. Using preconditioning, depending on the situation, the number of iterations required in a standard computation may be reduced from hundreds of iterations to fewer than 10. Preconditioning is critically important since the flow field must be determined for each step of a Newton iteration for determining the immersed body location.

At $t = 0$ we select the initial director field θ^0 as its equilibrium state absent fluid flow, as found by relaxing the system to a static configuration with the velocity field set to zero. With this initial director field we solve for the instantaneous initial velocity yield, $\mathbf{v}^0$. For the first time step we simply take as first extrapolations $\tilde{\mathbf{v}}^1 = \mathbf{v}^0$ and $\tilde{\theta}^1 = \theta^0$.

6.1. Newton iteration for $\mathbf{X}^{n+1}$

Following Ref. [78], the body position is updated by interpolation of the velocity field (assuming a no-slip boundary condition) via a backward Euler approximation,

$$\mathbf{X}^{n+1} = \mathbf{X}^n + \Delta t (S_h^n)^*\left[\mathbf{v}^{n+1}\left(\mathbf{A}(\mathbf{X}^{n+1})\right)\right], \tag{63}$$

where $\mathbf{A}(\mathbf{X})$ is on the right hand side of Eq. (56), and which depends on a surface force density $\mathbf{F}(\mathbf{X})$ and the anchoring angle $\phi(\mathbf{X})$. Equivalently, we wish to find the roots of the following nonlinear system:

$$\mathbf{G}(\mathbf{X}) = \mathbf{X} - \mathbf{X}^n - \Delta t (S_h^n)^*\left[\mathbf{v}^{n+1}(\mathbf{A}(\mathbf{X}))\right] = \mathbf{0}, \tag{64}$$

which we find using Newton–Raphson iteration. Given an initial guess $\mathbf{X}_0$, subsequent iterates $\mathbf{X}_k$ are updated as

$$\mathbf{X}_{k+1} = \mathbf{X}_k + \delta\mathbf{X}, \tag{65}$$

$$\text{where} \quad \mathbf{J}\,\delta\mathbf{X} = -\mathbf{G}(\mathbf{X}_k), \tag{66}$$

and $\mathbf{J} = [\partial\mathbf{G}/\partial\mathbf{X}](\mathbf{X}_k)$. Fortunately, $\mathbf{v}^{n+1}$ is linear in $\mathbf{A}(\mathbf{X}^{n+1})$, so we have neatly that

$$\mathbf{J}\delta\mathbf{X} = \delta\mathbf{X} - \Delta t (S_h^n)^*\left[\mathbf{v}^{n+1}\left(\mathbf{J}_A\delta\mathbf{X}\right)\right], \tag{67}$$

where $\mathbf{J}_A = [\partial\mathbf{A}/\partial\mathbf{X}](\mathbf{X}_k)$. With the inclusion of complex surface forces (e.g. elastic forces) and anchoring conditions, however, the analytical description of the Jacobian $\mathbf{J}_A$ is not a simple task, and numerical differentiation is slow. Instead we use the following approximation:

$$\mathbf{J}_A\delta\mathbf{X} \approx \frac{1}{\varepsilon}\left(\mathbf{A}(\mathbf{X}_k + \varepsilon\delta\mathbf{X}) - \mathbf{A}(\mathbf{X}_k)\right), \tag{68}$$

where we set $\varepsilon = 10^{-6}$ [84]. Now Eq. (66) is solved by GMRES iteration, usually taking only a few iterative steps to converge even without a preconditioner.

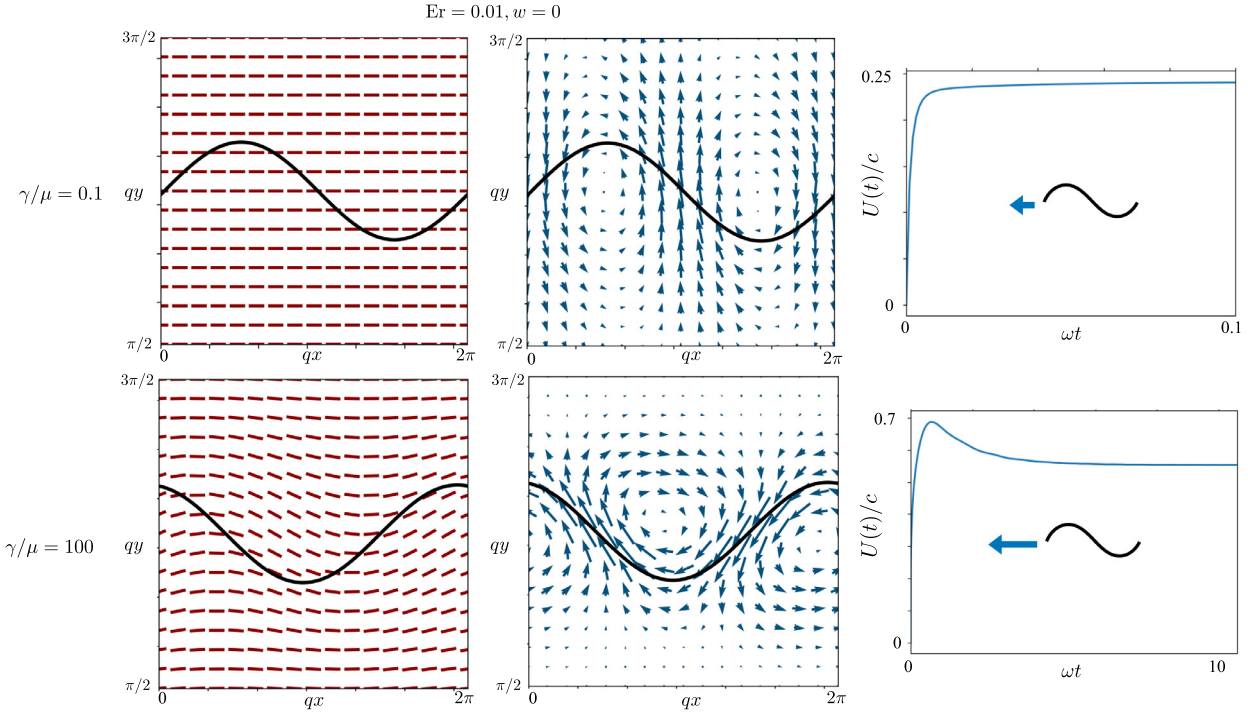

Fig. 4. Director fields (left panels) and velocity fields in the lab frame (center panels) at small Ericksen number, with zero anchoring strength, for both small (top panels) and large (bottom panels) rotational viscosity. Only part of the periodic computational domain (with dimensions $(L_x, L_y) = (2\pi, 4\pi)$) is shown. The swimming speed (right panels) is considerably increased at large rotational viscosity and the flow is bound to a region local to the swimmer. Arrows there indicate the direction of swimming; the direction of wave propagation is to the right. The results are consistent with the analytical results derived in Ref. [55].

6.2. *Tethering to ghost points for bodies with specified shape or gait*

A standard approach in the immersed boundary framework is to connect surface material points to target ghost points $\mathbf{Z}(t)$ using "springs" with stiffness k. In the event that the surface position is prescribed, we define the force density

$$\mathbf{F}(\mathbf{X}^{n+1}) = -k(\mathbf{X}^{n+1} - \mathbf{Z}^{n+1}), \tag{69}$$

where $\mathbf{Z}^{n+1} = \mathbf{Z}(t_{n+1})$ is specified. The preferred molecular direction on the surface is computed on the target surface $\phi(\mathbf{X}^{n+1}) = \phi(\mathbf{Z}(t_{n+1}))$, and the right hand side of Eq. (56) simplifies with $\mathbf{A}(\mathbf{X}^{n+1}) = \mathbf{0}$ and

$$\mathbf{B} = \begin{pmatrix} -S_h^n\left[\mathbf{F}(\mathbf{Z}^{n+1})\right] - w\nabla\cdot\mathbf{R}(\tilde{\theta}^{n+1})S_h^n\left[\phi(\mathbf{Z}^{n+1})\right] - w\mathbf{R}(\tilde{\theta}^{n+1})\cdot\nabla S_h^n\left[\phi(\mathbf{Z}^{n+1})\right] \\ \theta^n + \Delta t N\left(\tilde{\mathbf{v}}^{n+1}, \tilde{\theta}^{n+1}\right) + \dfrac{w\Delta t}{\gamma' \mathrm{Er}} S_h^n\left[\phi(\mathbf{Z}^{n+1})\right] \end{pmatrix}. \tag{70}$$

At each timestep, a constant velocity is added to the target shape $\mathbf{Z}$ which is selected to ensure zero net force in the periodic domain.

In the present work we will be interested in a surface deformation associated with a swimming body of infinite length, which combines a prescribed undulatory gait and the resulting rigid body motion from the constraint of zero net force (a neutrally buoyant swimmer; see [64]). Writing the prescribed gait as $\mathbf{Z}(t)$, the surface moves with speed $\mathbf{X}_t = \mathbf{Z}_t + \mathbf{U}$, where $\mathbf{U}$ is the unknown swimming speed, and the tethering forces at time t_{n+1} are approximated as

$$\mathbf{F}(\mathbf{X}^{n+1}) = -k(\mathbf{X}^{n+1} - \mathbf{Z}^{n+1} - \Delta t\mathbf{U}^{n+1}). \tag{71}$$

In the nonlinear system of equations $\mathbf{G}(\mathbf{X}) = \mathbf{0}$ shown in Section 6.1 we now include the unknown swimming velocity $\mathbf{U}^{n+1}$ and the constraint of zero net force, $\int_0^L \mathbf{F}(\mathbf{X}^{n+1})\,ds = \mathbf{0}$. We require the tethering force to overcome the viscous drag on the surface, and based on inspection of Eq. (A.5) we set $k = 10^4$ Er in the simulations to come.

7. Large-amplitude swimming

We are now in a position to investigate swimming in a liquid crystal for large amplitude undulations, and in the presence of boundaries. We begin by returning to a setting with no confining boundaries to probe the following question. Does the unexpected transition from retrograde to prograde locomotion in an infinite fluid with large rotational viscosity and strong anchoring described in Ref. [55], which is based the small-amplitude asymptotic theory discussed in Section 4, persist at large amplitude? Or is it merely a mathematical oddity which appears at vanishingly small wave amplitude?

We consider the director and velocity fields generated by the motion of a swimmer of amplitude $a = 1$ at small Ericksen number (Er = 0.01), and we set $K_1 = K_3$ and $\mu_1 = \mu_2 = \mu$ and $\lambda = 0.75$ for the duration of the paper. Fig. 4 shows the director and velocity fields for zero anchoring strength and for both small and large rotational viscosity γ. The velocity field shown is that seen in the lab frame. The periodic computational domain has dimensions $(L_x, L_y) = (2\pi, 4\pi)$, and only part of the physical domain is shown. In both cases the swimmer moves to the left ($U > 0$), opposite the direction of the traveling wave, and the swimming speed is significantly increased at large rotational viscosity, in agreement with theory developed in Ref. [55] where a local maximum in swimming speed was found for roughly this parameter set. Contributing to the increased swimming speed at large rotational viscosity, we see that the director field is significantly disturbed by the body motion, even with no anchoring strength, and the associated forcing results in a recirculating zone between wavecrests. The flow field in this case is tightly confined to the region local to the swimmer.

Fig. 5 addresses the same situation but with strong anchoring, $w = 10$. The strong anchoring condition causes a significant disturbance in the director field in both cases, and an increase in the swimming speed in the case of small rotational viscosity. It is at large rotational viscosity that we find the answer to the question posed at the beginning of this section: indeed, the transition to prograde motion, swimming in the same direction as wave passage ($U < 0$) is observed at large wave amplitude. The associated fluid flow is also striking, appearing as a plug flow, nearly uniform across the entire swimming body, and as in the case of zero anchoring strength, is primarily bound to a region near

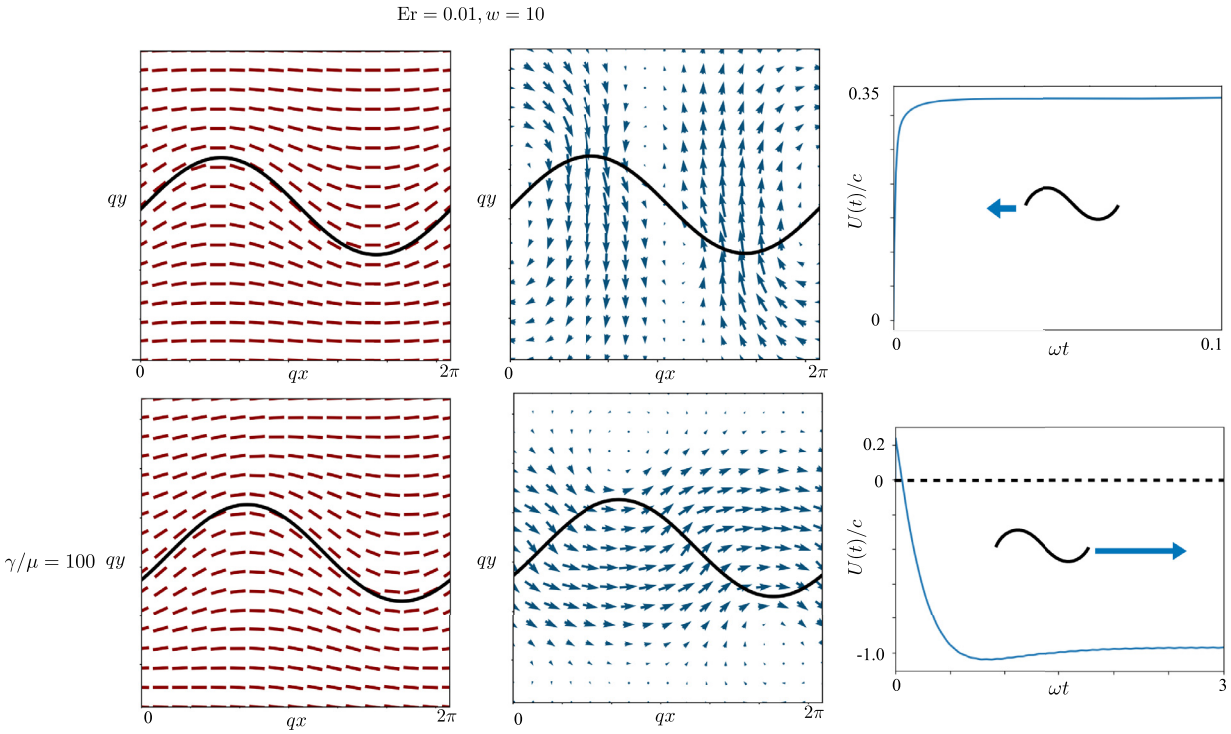

Fig. 5. Director fields (left panels) and velocity fields in the lab frame (center panels) at small Ericksen number, now with strong anchoring strength, for both small and large rotational viscosity. We verify at large swimming amplitude the reversal of swimming direction at large rotational viscosity predicted for small amplitude waves in Ref. [55], and find a plug-like flow in the direction of wave propagation in that regime.

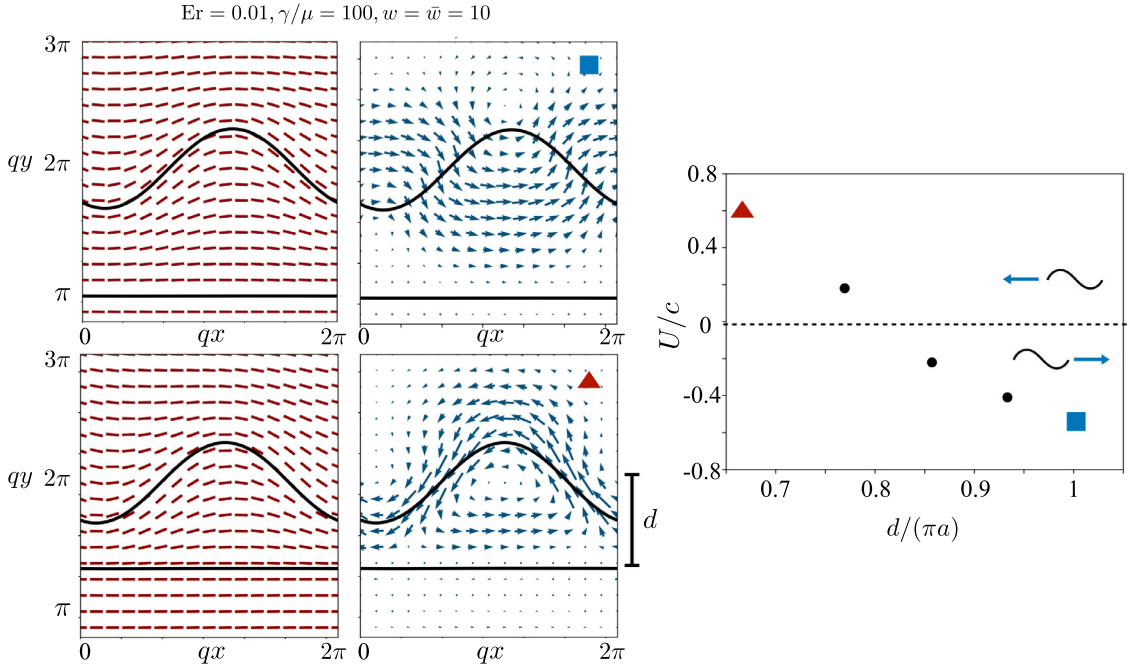

Fig. 6. Swimming in a wide channel but much nearer to one of the walls, at small Ericksen number, Er = 0.01, large rotational viscosity, $\gamma/\mu = 100$, and strong tangential anchoring conditions on both surfaces, $w = \bar{w} = 10$. The periodic computational domain has vertical length 4π. The panels on the left show the director and velocity fields for $d = \pi$ (top) and $d = 2\pi/3$ (bottom). Prograde swimming (to the right) when the wall is distant diminishes in speed as the wall is drawn closer to the swimmer, and eventually gives way to retrograde swimming (swimming to the left) when the wall is closer than a critical distance, consistent with the theory developed in the previous sections.

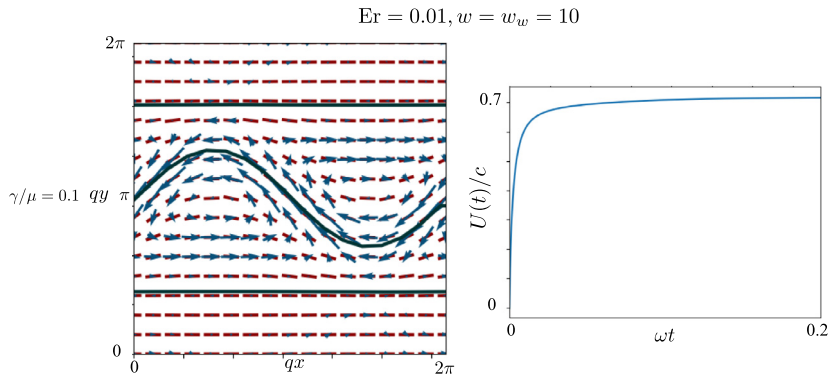

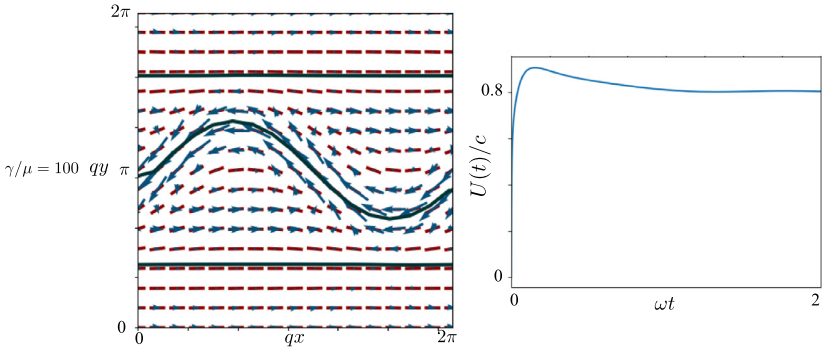

Fig. 7. Swimming in a channel at small Ericksen number, Er = 0.01, and strong anchoring, $w = \bar{w} = 10$, at small and large rotational viscosities. The director and velocity fields are overlaid (left panels), showing that the velocity is everywhere nearly aligned with the local director field, in stark contrast to the flow seen on the bottom of Fig. 5, where in the prograde motion the flow is roughly orthogonal to the director field. The right panels show the swimming speed as a function of time. With sufficient proximity to the channel walls the details of the liquid crystal become unimportant, and transport is similar to swimming in a confined Newtonian fluid.

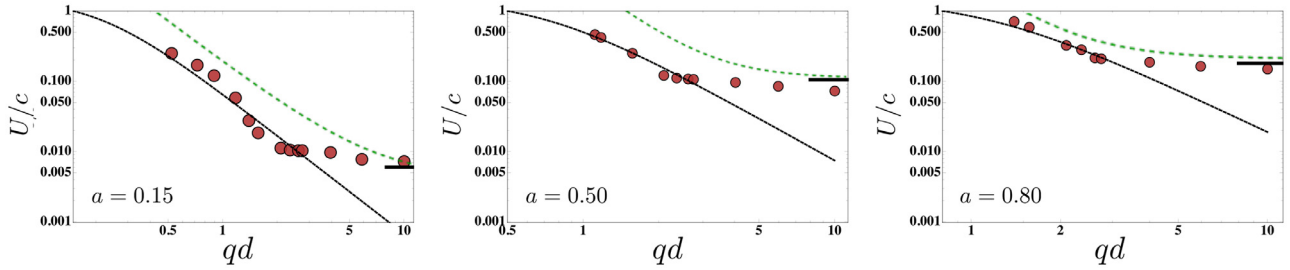

Fig. 8. The dimensionless swimming speed U/c versus the dimensionless channel width qd for small amplitude ($aq = 0.15$, left panel), medium amplitude ($aq = 0.50$, center panel), and large amplitude ($aq = 0.8$, right panel) undulations. Material parameters are $K_1 = K_3$, $\mu_1/\mu = \mu_2/\mu = 1$, $\gamma/\mu = 5$, Er = 1, and $\lambda = 0.75$. Dashed lines indicate: (black) the Katz result, Eq. (B.13) and (green) the Reynolds result, Eq. (2); solid lines indicate the unconfined swimming speed in a Newtonian fluid for the appropriate amplitude [85]. While three values of the anchoring strength ($w = \bar{w} = 0$, $w = \bar{w} = 1$, and $w = \bar{w} = 10$) were used, the differences in results were smaller than the size of the plot markers. (For interpretation of the references to colour in this figure legend, the reader is referred to the web version of this article.)

to the body only. Dynamics at Er = 1, not included here, also confirm the small amplitude theoretical results in Ref. [55]. Namely, the importance of anchoring strength is greatly diminished in determining the swimming speed, particularly at large rotational viscosity.

We now explore the effects of swimming in a wide channel but much nearer to a single wall. Numerically this is achieved by introducing a line of immovable target ghost springs. Fig. 6 shows the director and velocity fields, and swimming speeds at amplitude $a = 1$ and small Ericksen number, large rotational viscosity, and strong anchoring, $(\mathrm{Er}, \gamma/\mu, w) = (0.01, 100, 10)$. The wall has the same strong tangential anchoring condition as the body, $\bar{w} = 10$. The fields are shown for the cases $d = \pi$ (top) and $d = 2\pi/3$ (bottom). The prograde motion for free-space swimming remains when a distant wall is introduced, but when the wall is brought sufficiently close the motion reverts to retrograde motion, or swimming to the left, with a recirculating flow inside each wavecrest. The swimming speed appears to go through zero smoothly as a function of the distance to the wall, as theoretically predicted.

The symmetrized version of the geometry, closer to the theory developed in early sections, has walls above and below the swimmer, equally distant from its centerline. Fig. 7 shows the flow fields and director fields overlaid, for small and large rotational viscosity, and strong anchoring ($w = \bar{w} = 10$). Overlaying the two fields shows that the fluid velocity is almost perfectly aligned with the local director orientation, in stark contrast to the flow seen on the bottom of Fig. 5, where in the prograde motion the flow is nearly orthogonal to the director field close to the body. The recirculation zones are again prevalent, as seen near the wall in Fig. 6, and the dominant effect of the nearby walls in this case again remove the swimming direction reversal found in the study without walls: even at large rotational viscosity, in a channel the swimming speed is not far from that found for small rotational viscosity.

To further examine the robustness of our analytical results from Section 5 to large amplitude motion, we study swimming in a symmetric channel with variable stroke amplitude a and distance to the wall, d. In this section, we depart from the value Er = 0.01 used elsewhere in our numerical results, observing that if the Ericksen number is too small, however, the Eqs. (28)–(31) decouple, and it is harder to be sure that the numerics are validating our analysis. We therefore settle on Er = 1, which is close to what has been used in experiments. This value additionally preserves some effect of the anchoring strength on the swimming speed, so that we can verify that the role of anchoring strength

on swimming speed vanishes as d decreases. The results are shown in Fig. 8. While the Katz result (B.13) holds for $a/d \approx 1$, the speed quickly decreases to the unconfined speed, described in the small-amplitude case in Ref. [55]. However, the rate of decay for $a/d \approx 1$ is identical to the $(a/d)^{-2}$ factor observed by Katz, and the range of validity seems to extend to roughly $(a/d)^{-2} = 0.5$. Varying the material parameters confirms our analytical result that deep in the lubrication regime the liquid crystalline effects are swamped by mass conservation and the no-slip condition, which together imply that the swimming speed converges to the wave speed as $d \to a$. The numerical results also demonstrate that anchoring strength becomes unimportant in this regime (so long as the conditions on both swimmer and wall are tangential), which extends the results of Section 5.

Performing this calculation also gives us a glimpse at the speed of a finite-amplitude Taylor swimmer in an unbounded nematic solution, which is given by the limit $a/d \to 0$ for fixed a. Interestingly, despite previous findings that for the parameters used here a small-amplitude swimmer in a nematic swims faster than its Newtonian counterpart by a factor of roughly two [55], for larger amplitudes this trend is reversed. We can see this by comparing Fig. 8 to results from the literature on the Taylor swimmer in a Newtonian fluid beating with large-amplitude waves [85], which is given by horizontal black lines near $a/d = 0$. For the amplitudes used in Fig. 8, the Newtonian swimming speed is faster for $a = 0.5$ and $a = 0.8$ than the swimming speed in a liquid crystal.

8. Conclusion

This work extends previous studies of flagellated swimmers in unconfined liquid crystals and confined isotropic fluids to include both anisotropic and boundary effects. Our analytic results, based on asymptotic analysis in the stroke amplitude and channel width, suggest that the liquid-crystalline material properties have a diminishing effect on the swimming speed and volumetric flux as the width of the channel decreases, so long as the anchoring conditions on both surfaces are tangential. An extension of the model would include different anchoring conditions, such as homeotropic anchoring on one surface, and we suspect this would lead to very different results. In this setting the Ericksen–Leslie equations may break down and a Landau-de Gennes Q-tensor model would be more appropriate to study [39,86]. However, while the swimming speed is not dependent on liquid crystal parameters, the pressure, flux, and power consumption are strongly dependent on the rotational and anisotropic bulk viscosities. In our work we only considered the case of the swimmer moving parallel to the walls, and did not consider the torques which may tend to turn a swimmer [87–89]. The question of whether swimmers tend to be attracted or repelled to walls in a liquid crystal solution is probably best approached using squirmers [15,90] rather than Taylor's swimming sheet.

We also explored large amplitude swimming, made possible by the development of an immersed boundary method for nematic liquid crystals. We confirmed that the unexpected transition from retrograde to prograde locomotion at large rotational viscosity persists at large wave amplitude and is not an artifact of the small amplitude assumption. We also captured the return to retrograde motion in these cases when a nearby wall or channel is introduced. Interestingly, whereas in previous works swimmers with prescribed stroke at small amplitude have been shown to be faster than their Newtonian counterparts, for increasing amplitude this situation reverses, such that a swimmer is always locomoting at a slower speed and at greater power consumption than if it were locomoting in an isotropic, Newtonian fluid. Narrowing the channel also demonstrates an interesting connection between confinement and anchoring conditions.

We acknowledge helpful discussions with Marcelo Dias and Eric Lauga. This work was supported in part by National Science Foundation grants DMR 767-1121288 [UW MRSEC] and DMS-1661900 (SES) and CBET-1437195 (TRP). Part of this research was conducted using computational and visualization resources and services at the Center for Computation and Visualization, Brown University.

Appendix A. Single constant approximation in two dimensions

In two dimensions the transverse part of the molecular field is given by $\mathbf{h} = h\mathbf{n}^{\perp}$, with $\mathbf{n}^{\perp} = (-\sin\theta, \cos\theta)$. In the single constant approximation $K_1 = K_3$, we have $h = \nabla^2\theta$. The elastic stress is given by the bulk and anchoring contributions,

$$\boldsymbol{\sigma}^e + \boldsymbol{\sigma}^a = \left[-\theta_x^2 \hat{\mathbf{x}}\hat{\mathbf{x}} - \theta_y^2 \hat{\mathbf{y}}\hat{\mathbf{y}} - \theta_x\theta_y(\hat{\mathbf{x}}\hat{\mathbf{y}} + \hat{\mathbf{y}}\hat{\mathbf{x}})\right] + \nabla^2\theta\, \mathbf{R}(\theta), \tag{A.1}$$

where

$$\mathbf{R}(\theta) = \frac{1}{2}\Big\{ \lambda \sin 2\theta\, (\hat{\mathbf{x}}\hat{\mathbf{x}} - \hat{\mathbf{y}}\hat{\mathbf{y}}) + (1 - \lambda\cos 2\theta)\hat{\mathbf{x}}\hat{\mathbf{y}} - (1 + \lambda\cos 2\theta)\hat{\mathbf{y}}\hat{\mathbf{x}} \Big\}. \tag{A.2}$$

The total elastic force on the fluid is then

$$\mathbf{f}_e(\theta) = \nabla\cdot(\boldsymbol{\sigma}^e + \boldsymbol{\sigma}^s) = -\nabla^2\theta\,\nabla\theta - \frac{1}{2}\nabla\left(|\nabla\theta|^2\right) + \left(\nabla^2\theta\right)\nabla\cdot\mathbf{R}(\theta) + \mathbf{R}(\theta)\cdot\nabla\left(\nabla^2\theta\right), \tag{A.3}$$

where $\nabla^{\perp} = (\partial_y, -\partial_x)$ and

$$\nabla\cdot\mathbf{R}(\theta) = \lambda\left[\cos 2\theta(\hat{\mathbf{x}}\hat{\mathbf{x}} - \hat{\mathbf{y}}\hat{\mathbf{y}}) + \sin 2\theta(\hat{\mathbf{x}}\hat{\mathbf{y}} + \hat{\mathbf{y}}\hat{\mathbf{x}})\right]\cdot\nabla\theta. \tag{A.4}$$

The second term in Eq. (A.3) may be absorbed into the pressure.

The viscous stress may be written in the form

$$\boldsymbol{\sigma}^v(\mathbf{v};\theta) = (u_y - v_x)\left(A^{(2,0)}(\theta)\hat{\mathbf{x}}\hat{\mathbf{x}} + B^{(2,0)}(\theta)(\hat{\mathbf{x}}\hat{\mathbf{y}} + \hat{\mathbf{y}}\hat{\mathbf{x}}) + C^{(2,0)}(\theta)\hat{\mathbf{y}}\hat{\mathbf{y}}\right) \tag{A.5}$$

$$+u_x\left(A^{(1,1)}(\theta)\hat{\mathbf{x}}\hat{\mathbf{x}} + B^{(1,1)}(\theta)(\hat{\mathbf{x}}\hat{\mathbf{y}} + \hat{\mathbf{y}}\hat{\mathbf{x}}) + C^{(1,1)}(\theta)\hat{\mathbf{y}}\hat{\mathbf{y}}\right), \tag{A.6}$$

where we have used $\nabla\cdot\mathbf{v} = u_x + v_y = 0$. The coefficient functions of θ are viscosity dependent and are given by (with $\mu_1^* = \mu_1/\mu$, $\mu_2^* = \mu_2/\mu$, and $\gamma^* = \gamma/\mu$),

$$A^{(2,0)}(\theta) = \frac{1}{2}\sin(2\theta)\left(\mu_1^*\cos(2\theta) + \mu_1^* + \mu_2^*\right), \tag{A.7}$$

$$A^{(1,1)}(\theta) = \frac{1}{2}\left(4 + 2\left(\mu_1^* + \mu_2^*\right)\cos(2\theta) + \mu_1^*\cos(4\theta) + \mu_1^* + 2\mu_2^*\right), \tag{A.8}$$

$$B^{(2,0)}(\theta) = -\frac{1}{4}\left(\mu_1^*\cos(4\theta) - \mu_1^* - 2(\mu_2^* + 2)\right), \tag{A.9}$$

$$B^{(1,1)}(\theta) = \frac{1}{2}\mu_1^*\sin(4\theta), \tag{A.10}$$

$$C^{(2,0)}(\theta) = -\frac{1}{2}\sin(2\theta)\left(\mu_1^*\cos(2\theta) - \mu_1^* - \mu_2^*\right), \tag{A.11}$$

$$C^{(1,1)}(\theta) = -\frac{1}{2}\left(4 - 2\left(\mu_1^* + \mu_2^*\right)\cos(2\theta) + \mu_1^*\cos(4\theta) + \mu_1^* + 2\mu_2^*\right). \tag{A.12}$$

The viscous stress is symmetric, as expected. Finally, dotting the director field evolution equation (Eq. (10)) with $\mathbf{n}^{\perp}$ we find an evolution equation for the director field orientation angle,

$$\theta_t + \mathbf{v}\cdot\nabla\theta + \frac{1}{2}(u_y - v_x) = \lambda\left(\frac{\cos 2\theta}{2}(u_y + v_x) - \sin 2\theta\, u_x\right) + \frac{1}{\gamma^*\,\mathrm{Er}}\nabla^2\theta. \tag{A.13}$$

Appendix B. Details of the lubrication calculation for swimming speed

Here we calculate the flow field and swimming velocity for a swimmer near a wall in a nematic liquid crystal, using the lubrication approximations of Section 5. The liquid crystalline factors play a limited role and the calculation follows the same steps as in the isotropic case; we follow the approach of Pak and Lauga [59]. The lubrication approximation implies that the pressure $\tilde{p}$ is independent of $\tilde{y}$: $\tilde{p} = \tilde{p}(\tilde{x}, \tilde{t})$. With this assumption, the x-component of the velocity may be found in terms

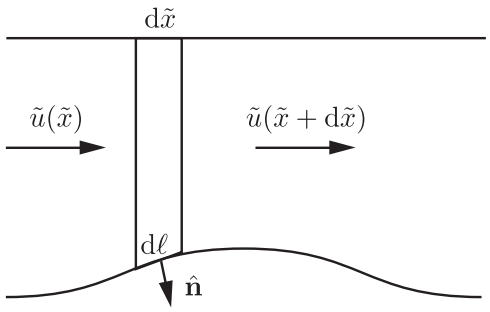

Fig. B.1. Incompressibility of the liquid crystal implies there is no net flow into or out of the slice.

of the pressure gradient from Eq. (36) and the no-slip boundary conditions (32)–(33):

$$\tilde{u} = \frac{\partial\tilde{p}/\partial\tilde{x}}{2[1+\gamma/(4\mu)]}\big(\tilde{y}-\tilde{Y}\big)(\tilde{y}-1) + \tilde{U}\frac{\tilde{y}-\tilde{Y}}{1-\tilde{Y}}, \tag{B.1}$$

where $\tilde{Y} = \tilde{a}\sin(x-t)$ and $\tilde{a} = a/d$. The complete $\tilde{x}$- and $\tilde{t}$- dependence of $\tilde{u}$ is still unknown because we don't yet know how $\tilde{p}$ depends on $\tilde{x}$ and $\tilde{t}$.

We can determine $\partial\tilde{p}/\partial\tilde{x}$ up to an unknown time-dependent constant by appealing to the conservation of volume of fluid. The net flow out of a slice of small thickness $\mathrm{d}\tilde{x}$ must vanish, as shown in Fig. B.1:

$$\int_{\tilde{Y}(\tilde{x}+\mathrm{d}\tilde{x})}^{1}\tilde{u}(\tilde{x}+\mathrm{d}\tilde{x})\mathrm{d}\tilde{y} - \int_{\tilde{Y}(\tilde{x})}^{1}\tilde{u}(\tilde{x})\mathrm{d}\tilde{y} + \tilde{\mathbf{v}}\cdot\hat{\mathbf{n}}\mathrm{d}\ell = 0, \tag{B.2}$$

where $\hat{\mathbf{n}}$ is the outward-pointing normal (Fig. B.1). Since $\tilde{\mathbf{v}}\cdot\hat{\mathbf{n}}\mathrm{d}\ell = -\tilde{v}(\tilde{x},\tilde{Y})\mathrm{d}\tilde{x}$ via the no-slip boundary conditions, we can rewrite (B.2) in differential form

$$\frac{\mathrm{d}}{\mathrm{d}\tilde{x}}\int_{\tilde{Y}}^{1}\tilde{u}(\tilde{x})\mathrm{d}\tilde{y} - \tilde{v}(\tilde{Y}) = 0, \tag{B.3}$$

or,

$$\int_{\tilde{Y}}^{1}\tilde{u}(\tilde{x})\mathrm{d}\tilde{y} + \tilde{a}\sin(\tilde{x}-\tilde{t}) = Q(\tilde{t}), \tag{B.4}$$

where $Q(\tilde{t})$ is to be determined. Using Eq. (B.1) for $\tilde{u}(\tilde{x})$, performing the integral in (B.4), and solving for $\partial\tilde{p}/\partial\tilde{x}$ yields

$$\frac{1}{\beta}\frac{\partial\tilde{p}}{\partial\tilde{x}} = \frac{12(1-Q)}{(1-\tilde{Y})^3} + 6\frac{\tilde{U}-2}{(1-\tilde{Y})^2}. \tag{B.5}$$

The only difference between this expression and the corresponding expression in the isotropic problem [59] is the factor of β [Eq. (37)], which contains all the dependence on the liquid crystalline material parameters. We can get an equation involving Q and $\tilde{U}$ only by integrating the pressure gradient over a period in $\tilde{x}$, and noting that the pressure must be periodic. Thus,

$$12I_3(1-Q) + 6I_2(\tilde{U}-2) = 0, \tag{B.6}$$

where

$$I_2 = \int_0^{2\pi}\frac{\mathrm{d}\tilde{x}}{[1-\tilde{Y}]^2} = \frac{2\pi}{(1-\tilde{a}^2)^{3/2}}, \tag{B.7}$$

$$I_3 = \int_0^{2\pi}\frac{\mathrm{d}\tilde{x}}{[1-\tilde{Y}]^3} = \frac{2\pi(2+\tilde{a}^2)}{(1-\tilde{a}^2)^{5/2}}. \tag{B.8}$$

Note that the prefactor involving the liquid crystalline parameters has dropped out, and the relation (B.6) is the same as in the isotropic case [59].

To get another equation involving q and $\tilde{U}$, we demand that the force on the swimmer vanish. It is simpler and equivalent to demand that the force on the wall at $\tilde{y} = 1$ vanishes,

$$\int_0^{2\pi}\sigma_{xy}(\tilde{y}=1)\mathrm{d}\tilde{x} = 0. \tag{B.9}$$

According to the lubrication scaling, the stress to leading order is given by

$$\tilde{\sigma}_{\tilde{x}\tilde{y}} = \big(1+\mu^*/2\big)\frac{\partial\tilde{u}}{\partial\tilde{y}}. \tag{B.10}$$

Integrating the stress leads to

$$(4\tilde{U}-6)I_1 + 6(1-Q)I_2 = 0, \tag{B.11}$$

where

$$I_1 = \int_0^{2\pi}\frac{\mathrm{d}\tilde{x}}{1-\tilde{Y}} = \frac{2\pi}{(1-\tilde{a}^2)^{1/2}}. \tag{B.12}$$

Since the liquid-crystalline factors in β have again dropped out, solving Eqs. (B.6) and (B.11) yields $Q = \tilde{U}$, and the isotropic swimming speed [4]:

$$\tilde{U} = \frac{3\tilde{a}^2}{2\tilde{a}^2+1}. \tag{B.13}$$

Denoting the time average over a period by angle brackets, the average flux entrained by the swimmer is given by $\langle\int_{\tilde{Y}}^{1}\tilde{u}\mathrm{d}\tilde{y}\rangle = \langle Q\rangle = \tilde{U}$.

Now that we have solved for Q and $\tilde{U}$, we can find the flow field. The flow field is a quadratic polynomial in $\tilde{y}$:

$$\tilde{u} = \frac{(y-\tilde{Y})\big\{6(1-y)\tilde{Y} - \tilde{U}\big[4+\tilde{Y}+\tilde{Y}^2-3y(1+\tilde{Y})\big]\big\}}{(\tilde{Y}-1)^3}. \tag{B.14}$$

Likewise we can find the angle field by integrating Eq. (28):

$$\tilde{\theta} = \alpha\frac{\tilde{y}-1}{(\tilde{Y}-1)^3}\Big\{\frac{\partial\tilde{Y}}{\partial\tilde{x}}(\tilde{Y}-1)^2 + (y-\tilde{Y})\big[\tilde{Y}(1-2\tilde{y}+\tilde{Y}) + \tilde{U}(-1+\tilde{y}+\tilde{y}\tilde{Y}-\tilde{Y}^2\big]\Big\}, \tag{B.15}$$

where

$$\alpha = \gamma^*\frac{K_3}{K_1}\mathrm{Er}\frac{1-\lambda}{2}. \tag{B.16}$$

References

[1] E. Lauga, T.R. Powers, The hydrodynamics of swimming microorganisms, Rep. Prog. Phys. 72 (2009) 096601.
[2] G.I. Taylor, Analysis of the swimming of microscopic organisms, Proc. R. Soc. Lond. Ser. A **209** (1951) 447–461.
[3] A.J. Reynolds, The swimming of minute organisms, J. Fluid Mech. 23 (1965) 241–260.
[4] D.F. Katz, On the propulsion of micro-organisms near solid boundaries, J. Fluids Mech. 64 (1974) 33.
[5] E. Lauga, Propulsion in a viscoelastic fluid, Phys. Fluids 19 (2007) 083104.
[6] N.J. Balmforth, D. Coombs, S. Pachmann, Microelastohydrodynamics of swimming organisms near solid boundaries in complex fluids, Q. J. Mech. Appl. Math. 63 (2010) 267.
[7] J.C. Chrispell, L.J. Fauci, M. Shelley, An actuated elastic sheet interacting with passive and active structures in a viscoelastic fluid, Phys. Fluids 25 (2013) 013103.
[8] A.A. Evans, E. Lauga, Propulsion by passive filaments and active flagella near boundaries, Phys. Rev. E 82 (2010) 041915.
[9] L.J. Fauci, A. McDonald, Sperm motility in the presence of boundaries, Bull. Math. Biol. 57 (1995) 679–699.
[10] D.J. Smith, E.A. Gaffney, J.R. Blake, J.C. Kirkman-Brown, Human sperm accumulation near surfaces: a simulation study, J. Fluid Mech. 621 (2009) 289–320.
[11] B. Liu, K.S. Breuer, T.R. Powers, Propulsion by a helical flagellum in a capillary tube, Phys. Fluids 26 (2014) 011701.
[12] L. Li, S.E. Spagnolie, Swimming and pumping by helical waves in viscous and viscoelastic fluids, Phys. Fluids 27 (2015) 021902.
[13] R. Ledesma-Aguilar, J.M. Yeomans, Enhanced motility of a microswimmer in rigid and elastic confinement, Phys. Rev. Lett. 111 (2013) 138101.
[14] M.A. Dias, T.R. Powers, Swimming near deformable membranes at low Reynolds number, Phys. Fluids 25 (2013) 101901.
[15] S.E. Spagnolie, E. Lauga, Hydrodynamics of self-propulsion near a boundary: predictions and accuracy of far-field approximations, J. Fluid Mech. 700 (2012) 105–147.
[16] L. Zhu, E. Lauga, L. Brandt, Low-Reynolds-number swimming in a capillary tube, J. Fluid Mech. 726 (2013) 285–311.
[17] J. Elgeti, G. Gompper, Wall accumulation of self-propelled spheres, Europhys. Lett. 101 (4) (2013) 48003.
[18] A. Zöttl, H. Stark, Hydrodynamics determines collective motion and phase behavior of active colloids in quasi-two-dimensional confinement, Phys. Rev. Lett. 112 (2014) 118101.
[19] K. Schaar, A. Zöttl, H. Stark, Detention times of microswimmers close to surfaces: influence of hydrodynamic interactions and noise, Phys. Rev. Lett. 115 (2015) 038101.

[20] G.J. Li, A. Karimi, A.M. Ardekani, Effect of solid boundaries on swimming dynamics of microorganisms in a viscoelastic fluid, Rheologica Acta 53 (2014) 911–926.
[21] S. Yazdi, A. Ardekani, A. Borhan, Swimming dynamics near a wall in a weakly elastic fluid, J. Nonlinear Sci. 25 (2015) 1153–1167.
[22] P. Galajda, J. Keymer, P. Chaikin, R. Austin, A wall of funnels concentrates swimming bacteria, J. Bacteriol. 189 (2007) 8704–8707.
[23] M.B. Wan, C.J.O. Reichhardt, Z. Nussinov, C. Reichhardt, Rectification of swimming bacteria and self-driven particle systems by arrays of asymmetric barriers, Phys. Rev. Lett. 101 (2008) 018102.
[24] J. Tailleur, M.E. Cates, Sedimentation, trapping, and rectification of dilute bacteria, Europhys. Lett. 86 (2009) 60002.
[25] J. Elgeti, G. Gompper, Self-propelled rods near surfaces, EPL (Europhys. Lett.) 85 (2009) 38002.
[26] J. Elgeti, U.B. Kaupp, G. Gompper, Hydrodynamics of sperm cells near surfaces, Biophys. J. 99 (2010) 1018–1026.
[27] R. Di Leonardo, L. Angelani, D. Dell'Arciprete, G. Ruocco, V. Iebba, S. Schippa, M.P. Conte, F. Mecarini, F. De Angelis, E. Di Fabrizio, Bacterial ratchet motors, Proc. Natl. Acad. Sci. USA 107 (2010) 9541–9545.
[28] I. Berdakin, Y. Jeyaram, V.V. Moshchalkov, L. Venken, S. Dierckx, S.J. Vanderleyden, A.V. Silhanek, C.A. Condat, V.I. Marconi, Influence of swimming strategy on microorganism separation by asymmetric obstacles, Phys. Rev. E 87 (2013) 052702.
[29] D. Takagi, J. Palacci, A.B. Braunschweig, M.J. Shelley, J. Zhang, Hydrodynamic capture of microswimmers into sphere-bound orbits, Soft Matter 10 (2014) 1784–1789.
[30] S.E. Spagnolie, C. Wahl, J. Lukasik, J.-L. Thiffeault, Microorganism billiards, Physica D 341 (2017) 33–44.
[31] M.S. Krieger, Microorganism billiards in closed plane curves, Europhys. J. E 39 (2016) 112–124.
[32] S.E. Spagnolie, G.R. Moreno-Flores, D. Bartolo, E. Lauga, Geometric capture and escape of a microswimmer colliding with an obstacle, Soft Matter 11 (2015) 3396–3411.
[33] A. Wysocki, J. Elgeti, G. Gompper, Giant adsorption of microswimmers: duality of shape asymmetry and wall curvature, Phys. Rev. E 91 (5) (2015) 050302.
[34] A.T. Brown, I.D. Vladescu, A. Dawson, T. Vissers, J. Schwarz-Linek, J.S. Lintuvuori, W.C.K. Poon, Swimming in a crystal, Soft Matter 12 (2016) 131.
[35] M.S. Davies Wykes, X. Zhong, J. Tong, T. Adachi, Y. Liu, L. Ristroph, M.D. Ward, M.J. Shelley, J. Zhang, Guiding microscale swimmers using teardrop-shaped posts, Soft Matter 13 (2017) 4681.
[36] J. Elgeti, R.G. Winkler, G. Gompper, Physics of microswimmers - single particle motion and collective behavior: a review, Rep. Prog. Phys. 78 (5) (2015) 056601.
[37] A. Zöttl, H. Stark, Emergent behavior in active colloids, J. Phys. 28 (25) (2016) 253001.
[38] C. Bechinger, R. Di Leonardo, H. Löwen, C. Reichhardt, G. Volpe, G. Volpe, Active particles in complex and crowded environments, Rev. Mod. Phys. 88 (4) (2016) 045006.
[39] P.G. de Gennes, J. Prost, The Physics of Liquid Crystals, 2nd, Oxford University Press, Oxford, 1995.
[40] A. Kumar, T. Galstian, S. Pattanayek, S. Rainville, The motility of bacteria in an anisotropic liquid environment, Mol. Cryst. Liq. Cryst. 574 (1) (2013) 33–39.
[41] P.C. Mushenheim, R.R. Trivedi, H.H. Tuson, D.B. Weibel, N.L. Abbott, Dynamic self-assembly of motile bacteria in liquid crystals, Soft Matter 10 (2014) 88–95.
[42] S. Zhou, A. Sokolov, O.D. Lavrentovich, I.S. Aranson, Living liquid crystals, Proc. Natl. Acad. Sci. USA 111 (2014) 1265–1270.
[43] A. Sokolov, S. Zhou, O.D. Lavrentovich, I.S. Aranson, Individual behavior and pairwise interactions between microswimmers in anisotropic liquid, Phys. Rev. E 91 (2015) 013009.
[44] R.R. Trivedi, R. Maeda, N.L. Abbott, S.E. Spagnolie, D.B. Weibel, Bacterial transport of colloids in liquid crystalline environments, Soft Matter (2015).
[45] J. Toner, H. Löwen, H.H. Wensink, Following fluctuating signs: anomalous active superdiffusion of swimmers in anisotropic media, Phys. Rev. E 93 (6) (2016) 062610.
[46] M.M. Genkin, A. Sokolov, O.D. Lavrentovich, I.S. Aranson, Topological defects in a living nematic ensnare swimming bacteria, Phys. Rev. X 7 (1) (2017) 011029.
[47] I.I. Smalyukh, J. Butler, J.D. Shrout, M.R. Parsek, G.C.L. Wong, Elasticity-mediated nematiclike bacterial organization in model extracellular dna matrix, Phys. Rev. E 78 (2008) 030701(R).
[48] D. Nishiguchi, K.H. Nagai, H. Chaté, M. Sano, Long-range nematic order and anomalous fluctuations in suspensions of swimming filamentous bacteria, Phys. Rev. E 95 (2017) 020601(R).
[49] C. Viney, A.E. Huber, P. Verdugo, Liquid crystalline order in mucus, Macromolecules 26 (4) (1993) 852–855.
[50] L.S. M. A. Fritz, Clinical Gynecologic Endocrinology and Infertility, 8, Lippincott Williams & Wilkins, 2011.
[51] F.C. Chretien, Involvement of the glycoproteic meshwork of cervical mucus in the mechanism of sperm orientation, Acta Obstet. Gynecol. Scand. 82 (2003) 449–461.
[52] I.W. Hamley, Liquid crystal phase formation by biopolymers, Soft Matter 6 (9) (2010) 1863–1871.
[53] M.S. Krieger, S.E. Spagnolie, T.R. Powers, Locomotion and transport in a hexatic liquid crystal, Phys. Rev. E 90 (2014) 052503.
[54] M.S. Krieger, M.A. Dias, T.R. Powers, Minimal model for transient swimming in a liquid crystal, Eur. Phys. J. E 38 (2015) 94.
[55] M.S. Krieger, S.E. Spagnolie, T.R. Powers, Microscale locomotion in a nematic liquid crystal, Soft Matter 11 (2015) 9115–9125.
[56] A. Sengupta, S. Herminghaus, C. Bahr, Liquid crystal microfluidics: surface, elastic and viscous interactions at microscales, Liq. Cryst. Rev. 2 (2014) 73–110.
[57] S. Shi, H. Yokoyama, Liquid crystal foams generated by pressure-driven microfluidic devices, Langmuir 31 (2015) 4429–4434.
[58] C. Peng, Y. Guo, C. Conklin, J. Viñals, S.V. Shiyanovskii, Q.-H. Wei, O.D. Lavrentovich, Liquid crystals with patterned molecular orientation as an electrolytic active medium, Phys. Rev. E 92 (2015) 052502.
[59] O. Pak, E. Lauga, Theoretical models in low-Reynolds number locomotion, in: C. Duprat, H. Stone (Eds.), Low-Reynolds-Number Flows: Fluid-Structure Interactions, Royal Society of Chemistry, 2014, p. 100.
[60] L.D. Landau, E.M. Lifshitz, Theory of Elasticity, 3rd, Pergamon Press, Oxford, 1986.
[61] R.G. Larson, The Structure and Rheology of Complex Fluids, Oxford University Press, New York, 1999.
[62] X. Yao, Studies on lyotropic chromonic liquid crystals in nematic and biphasic regions, Georgia Institute of Technology, Atlanta, GA, 2011 Ph.D. thesis.
[63] P.C. Mushenheim, R.R. Trivedi, D.B. Weibel, N.L. Abbott, Using liquid crystals to reveal how mechanical anisotropy changes interfacial behaviors of motile bacteria, Biophys. J. 107 (2014) 255–265.
[64] E. Lauga, T. Powers, The hydrodynamics of swimming microorganisms, Rep. Prog. Phys. 72 (2009) 096601.
[65] S. Zhou, K. Neupane, Y. Nastishin, A. Baldwin, S. Shiyanovskii, O. Lavrentovich, S. Sprunt, Elasticity, viscosity, and oriental fluctuations of a lyotropic chromonic nematic liquid crystal disodium cromoglycate, Soft Matter 10 (1) (2014) 6571–6581.
[66] E. Lauga, Propulsion in a viscoelastic fluid, Phys. Fluids 19 (2007) 083104.
[67] D.J. Smith, E.A. Gaffney, H. Gadêlha, N. Kapur, J.C. Kirkman-Brown, Bend propagation in the flagella of migrating human sperm, and its modulation by viscosity, Cell Mot. Cyto. 66 (4) (2009) 220–236.
[68] G.J. Elfring, G. Goyal, The effect of gait on swimming in viscoelastic fluids, J. Non-Newtonian Fluid Mech. 234 (2016) 8–14.
[69] G.J. Elfring, E. Lauga, Synchronization of flexible sheets, J. Fluid Mech. 674 (2011) 163–173.
[70] L.J. Cummings, T.-S. Lin, L. Kondic, Modeling and simulations of the spreading and destabilization of nematic droplets, Phys. Fluids 23 (2011) 043102.
[71] C. Peskin, The immersed boundary method, Acta Numer. 11 (2002) 479–517.
[72] J. Teran, L. Fauci, M. Shelley, Viscoelastic fluid response can increase the speed and efficiency of a free swimmer, Phys. Rev. Lett. 104 (2010) 038101.
[73] B. Thomases, R.D. Guy, Mechanisms of elastic enhancement and hindrance for finite-length undulatory swimmers in viscoelastic fluids, Phys. Rev. Lett. 113 (2014) 098102.
[74] R.D. Guy, B. Thomases, Computational challenges for simulating strongly elastic flows in biology, in: Complex Fluids in Biological Systems, Springer, 2015, pp. 359–397.
[75] P. Lee, C.W. Wolgemuth, An immersed boundary method for two-phase fluids and gels and the swimming of caenorhabditis elegans through viscoelastic fluids, Phys. Fluids 28 (2016) 011901.
[76] C.J. Guido, J.P. Binagia, E.S.G. Shaqfeh, Three-dimensional simulations of undulatory and amoeboid swimmers in viscoelastic fluids, Soft Matter (2019).
[77] C.S. Peskin, The immersed boundary method, Acta Numerica 11 (2002) 479–517.
[78] R.D. Guy, B. Thomases, Computational challenges for simulating strongly elastic flows in biology, in: Complex Fluids in Biological Systems, Springer, 2015, pp. 359–397.
[79] J.M. Teran, C.S. Peskin, Tether force constraints in stokes flow by the immersed boundary method on a periodic domain, SIAM J. Sci. Comput. 31 (2009) 3404–3416.
[80] J. Teran, L. Fauci, M. Shelley, Viscoelastic fluid response can increase the speed and efficiency of a free swimmer, Phys. Rev. Lett. 104 (2010) 038101.
[81] D.B. Stein, R.D. Guy, B. Thomases, Immersed boundary smooth extension (IBSE): a high-order method for solving incompressible flows in arbitrary smooth domains, J. Comput. Phys. 335 (2017) 155–178.
[82] D.B. Stein, R.D. Guy, B. Thomases, Convergent solutions of stokes oldroyd-b boundary value problems using the immersed boundary smooth extension (ibse) method, J. Non-Newtonian Fluid Mech. 268 (2019) 56–65.
[83] B. Fornberg, A Practical Guide to Pseudospectral Methods, 1, Cambridge University Press, 1998.
[84] D.A. Knoll, D.E. Keyes, Jacobian-free Newton–Krylov methods: a survey of approaches and applications, J. Comput. Phys. 193 (2) (2004) 357–397.
[85] M. Sauzade, G.J. Elfring, E. Lauga, Taylor's swimming sheet: analysis and improvement of the perturbation series, Physica D 240 (2011) 1567–1573.
[86] A.M. Sonnet, P.L. Maffettone, E.G. Virga, Continuum theory for nematic liquid crystals with tensorial order, J. Non-Newtonian Fluid Mech. 119 (2004) 51–59.
[87] G. Cupples, R.J. Dyson, D.J. Smith, Viscous propulsion in active transversely-isotropic media, J. Fluid Mech. 812 (2017) 501.
[88] J. Shi, T.R. Powers, Swimming in an anisotropic fluid: how speed depends on alignment angle, Phys. Rev. Fluids 2 (2017) 123102.
[89] G. Cupples, R.J. Dyson, D.J. Smith, On viscous propulsion in active transversely-isotropic media, J. Fluid Mech. 855 (2018) 408.
[90] J.S. Lintuvuori, A. Würger, K. Stratford, Hydrodynamics defines stable swimming direction of spherical squirmers in a nematic liquid crystal, Phys. Rev. Lett. 119 (2017) 068001.